DISORDERED SYSTEMS AND OPTIMIZATION: *ELASTIC LINES AND RANDOM MAGNETS*

Viljo Petäjä

Laboratory of Physics
Helsinki University of Technology

Fysiikan laboratorio
Teknillinen korkeakoulu

DISSERTATION 140 (2006)

DISORDERED SYSTEMS AND OPTIMIZATION: ELASTIC LINES AND RANDOM MAGNETS

Viljo Petäjä

Laboratory of Physics
Helsinki University of Technology
Espoo, Finland

Dissertation for the degree of Doctor of Science in Technology to be presented with due permission of the Department of Engineering Physics and Mathematics, Helsinki University of Technology for public examination and debate in Auditorium E at Helsinki University of Technology (Espoo, Finland) on the 26th of April, 2006, at 16 o'clock.

Dissertations of Laboratory of Physics, Helsinki University of Technology
ISSN 1455-1802

Dissertation 140 (2006):
Viljo Petäjä: Disordered Systems and Optimization: Elastic Lines and Random Magnets
ISBN 951-22-8149-X (print)
ISBN 951-22-8150-3 (electronic)
URL http://lib.tkk.fi/Diss/2006/isbn9512281503

Picaset Oy
Helsinki 2006

Tiivistelmä

Nollalämpötilassa fysikaaliset systeemit ovat perustilassa, jonka ominaisuudet määräävät systeemin käyttäytymisen hyvin pitkälti myös äärellisissä lämpötiloissa. Yleisesti ottaen systeemin perustilaa vastaavan parametrijoukon löytäminen on vaativa laskennallinen tehtävä, joka vaikeutuu entisestään, jos systeemissä on sisäistä epäjärjestystä. Staattisen epäjärjestyksen tapauksessa perustila voidaan kuitenkin usein löytää tehokkaasti käyttäen kombinatorista optimointia. Tässä väitöskirjassa tutkitaan kahta tällaista systeemiä – suunnattuja polymeereja ja Isingin satunnaiskenttämallia.

Suunnatut polymeerit ovat viivamaisia joustavia objekteja, jotka kuvaavat muun muassa magneettisia vuoviivoja toisen tyypin suprajohteissa. Suprajohtavuuden säilymisen kannalta tärkeää on staattinen epäjärjestys, joka estää vuoviivoja liikkumasta sähkövirran aiheuttaman voiman alaisena. Myös vuoviivojen keskinäisen kietoutumisen uskotaan kasvattavan virran maksimiarvoa, joka voidaan johtaa suprajohteen läpi siten, että suprajohtavuus säilyy. Väitöskirjassa tutkitaan numeerisesti kaksi- ja kolmiulotteisten vuoviivasysteemien karhenemista, kolmiulotteisessa tapauksessa myös kietoutumista, ympäristöissä jotka sisältävät joko korreloimatonta piste-epäjärjestystä tai vinoja viivadefektejä. Piste-epäjärjestyksessä kahdessa ulottuvuudessa viivat karhenevat logaritmisesti systeemin leveyden kasvaessa, kun taas kolmessa ulottuvuudessa ne noudattavat satunnaiskävely -tyyppistä käytöstä. Kolmiulotteisista viivasysteemeistä tulee täysin kietoutuneita viivojen suuntaisen systeemin koon (korkeuden) ylitettyä tietyn kriittisen arvon. Numeeristen tulosten perusteella tämä transitio kuuluu tavallisen perkolaatiotransition luokkaan. Piste-epäjärjestyksessä viivojen perustila ei ole separoituva, eli perustilaan ei päästä lisäämällä viivoja systeemiin toisistaan riippumatta. Jos taas epäjärjestys koostuu viivadefekteistä, perustila on separoituva. Tämä johtaa satunnaiskävely -tyyppiseen viivojen karhenemiseen kahdessa ulottuvuudessa ja niin sanottuun ballistiseen käytökseen kolmessa ulottuvuudessa. Lisäksi, viivat kietoutuvat vain, jos systeemiin lisätään myös piste-epäjärjestystä.

Kombinatorisen optimoinnin käyttö perustilan laskemiseen edellyttää, että tutkittava fysikaalinen ongelma ensin kuvataan vastaavalle kombinatoriselle ongelmalle. Kaikissa tapauksissa tällaista kuvausta ei välttämättä edes löydy. Viime vuosina kvanttijäähdytys on kiinnostanut optimointimenetelmänä, joka on yhtä laajasti sovellettavissa kuin perinteinen simuloitu jäähdytys, mutta jonka uskotaan löytävän tutkittavan systeemin perustilan huomattavasti nopeammin. Tässä väitöskirjassa testataan kvanttijäähdytyksen toimivuutta yksi-, kaksi- ja kolmiulotteisen Isingin satunnaiskenttämallin tapauksessa.

Abstract

The behavior of many physical systems, especially at low temperatures, is governed by the properties of their ground states. Usually it is not a trivial task to find the ground state configuration, especially in the case of disordered, complex systems. However, with quenched disorder this can be often done efficiently with the means of combinatorial optimization. In this thesis we study two such problems – directed polymers and the random field Ising model.

Directed polymers are elastic line-like objects which provide a simple model for magnetic flux lines (vortices) in type-II superconductors. The pinning of flux lines by static disorder is crucial for sustaining the superconductivity upon the insertion of an external current. Also the topological entanglement of flux lines is believed to increase the maximal amount of the current that can be applied to the sample without losing superconductivity. We investigate the roughening of two- and three-dimensional systems of elastic lines in the presence of two types of randomness in the media: uncorrelated point-like disorder and splayed columnar defects. In addition, in three dimensions also the mutual entanglement of the lines is considered. For point disorder we find that the roughness of lines grows logarithmically with the increasing system width in two dimensions whereas in three dimensions lines exhibit random walk -like behavior. As the consequence of increasing wandering in three dimensions lines become completely entangled above the critical system height. Numerical evidence implies that this transition is in the ordinary percolation universality class. In point disorder the ground state is not separable, i.e. it can not be considered as a set of many independent lines. For splay disorder the ground state is separable leading to a random walk -like roughening in two dimensions and ballistic behavior in three dimensions. Furthermore, we find that in splay disorder lines exhibit the entanglement transition only when the original system is perturbed with point disorder.

When applying combinatorial optimization for finding the ground states of physical systems one has to find a mapping from the physical problem to the corresponding combinatorial one. This means that each case has to be treated individually. During the recent years quantum annealing has gained a lot of attention as a promising candidate for a common optimization method, like simulated annealing but with a promise of a faster convergence to the optimal configuration for a given problem. The random field Ising model serves as a test problem for the quantum annealing the performance of which is analyzed numerically in one, two and three dimensions.

Preface

The work reported in this thesis was carried out at the Laboratory of Physics at Helsinki University of Technology during the years 2001-2005.

I wish to express my gratitude to my advisor Docent Mikko Alava. Without his patient and inspiring guidance it would not have been possible to complete this work. I acknowledge Academy Professor Risto Nieminen for making it possible to work as a member of COMP and for giving the opportunity to undertake this thesis. I thank Professor Heiko Rieger for his invaluable help and mentoring throughout this project. Visiting him first in Cologne and later in Saarbrücken has always been very inspiring and motivating. I also wish to thank the former and current members of Professor Heiko Rieger's group for having good time and interesting discussions during my visits to Germany. I acknowledge Dr. Deok-Sun Lee for contributing to Publication II. Special thanks go to Thorsten Knetter and Gerd Schröder for familiarizing me with the local culture. I express my sincere appreciation to the people in Laboratory of Physics. I thank Dr. Eira Seppälä for her guidance in the early stages of my scientific work and MSc Matti Sarjala for the fruitful collaboration during the last few years. MSc Jari Rosti is acknowledged for many useful discussions and for his contribution to the great atmosphere in Mikko's research group.

I am very grateful to my parents and to my sister for encouraging and supporting me throughout my studies and work leading to this thesis. The last but not the least acknowledgments belong to Susanna for cheering me up when needed and keeping me going.

Otaniemi, January 2006

Viljo Petäjä

List of publications

This Thesis consists of an overview and the following publications:

I. V. Petäjä, M. Alava, and H. Rieger, "Ground states of two directed polymers," International Journal of Modern Physics C **12**, 421-436 (2001).

II. V. Petäjä, D.-S. Lee, M. Alava, and H. Rieger, "Collective roughening of elastic lines with hard core interaction in a disordered environment," Journal of Statistical Mechanics: Theory and Experiment, P10010 (2004) (17 pages).

III. V. Petäjä, M. Alava, and H. Rieger, "Entanglement transition of elastic lines in a strongly disordered environment," Europhysics Letters, **66** 778-784 (2004).

IV. V. Petäjä, M. Sarjala, M. Alava, and H. Rieger, "Elastic lines on splayed defects studied numerically ," Physical Review B **73**, 094517 (2006) (9 pages).

V. M. Sarjala, V. Petäjä, and M. Alava, "Optimization of random field Ising model by quantum annealing," Journal of Statistical Mechanics: Theory and Experiment, P01008 (2006) (13 pages).

The author's contribution

The author has had an active role in all phases of the research reported in this thesis. Most of the numerical calculations and the related programming work were carried out by the author. The calculations concerning the effects of disorder distribution in Publication II are due to Dr. Deok-Sun Lee. The construction of two-dimensional test systems for Publication IV and the majority of the calculations of Publication V were carried out by MSc. Matti Sarjala while instructed by the author. In Publications II and III the author has written the drafts for the sections presenting the numerical data and concerning technical details of the calculations. The manuscripts of Publications IV and V are mainly written by the author himself.

Contents

Chapter 1

Introduction

In a broad range of optimization problems one can identify a function of a configuration of problem variables which measures the quality of the given configuration. In physics the value of this function is recognized as the energy of the system. The space of all possible configurations spans the *energy landscape* associated with a given problem. Typically one is interested in the configuration that corresponds to the lowest energy state or *ground state*. The real physical systems fall into their ground state when the temperature is reduced to zero. Often the ground state properties govern the general system's behavior, especially at low temperature. Usually it is not a trivial task to find the ground state configuration, it depends on the complexity of the energy landscape of the problem. One could compare this to a hilly landscape where one has to find the the lowest lying spot. The shape of the hills determines the difficulty of this task.

In recent years it has been found that the ground states of many systems with quenched disorder are accessible numerically in polynomial time [1]. This gift is not for free: first a mapping of the problem of finding the exact ground state of the model Hamiltonian under consideration onto a standard combinatorial optimization problem has to be found. This means that each problem has to be treated individually. If one is lucky, a given problem falls into the P-class of problems which are solvable in polynomial time (i.e. required time increases at most polynomially with the size of the problem). If not, the problem is in NP-class[1] which means that the calculation time increases faster

[1]So far, there has not been found any algorithm that can solve a NP-class problem polynomially or faster. On the other hand there is also no proof – forth or against – whether such algorithms can exist at all.

than polynomially (exponentially, for instance) with the problem size. A classical example of such systems is the three dimensional Edward-Anderson spin-glass model [2, 3]. In practice this limits the numerical studies of such models to rather small system sizes which often are not sufficient for obtaining conclusive results.

Sometimes it is better to get a good approximation in reasonable time than wait for the exact ground state. A well known and widely used method for this purpose is *simulated annealing* [4] which mimics the real world cooling. In simulated annealing thermal fluctuations make it possible to escape from local minima configurations. During the annealing process the amplitude of the thermal fluctuations is gradually reduced which decreases the chance of unfavorable excitations and the system converges to the optimal configuration. However, many systems have very high inter-minima barriers which reduces heavily the transition probabilities. In these cases as the annealing time is increased the energy difference between the obtained configuration and the exact ground state decreases only logarithmically [5]. Simulated annealing can be, however, applied to a very broad range of optimization problems, including NP-class optimization problems, and it performs almost always with a same efficiency.

During the recent years *quantum annealing*, a possible application of *quantum computing* [6], has gained a lot of attention as a promising candidate for a method applicable for as wide range of problems as simulated annealing, with a promise of a faster convergence to the optimal configuration for a given problem. Instead of thermally overcoming the barriers one can now quantum mechanically tunnel through them.

This thesis considers two models of disordered systems – directed polymers (Chapter 2) and random field Ising model (Chapter 3). For both of them the exact ground state can be found in a polynomial time with the means of combinatorial optimization [1]. Directed polymers provide a simple model for magnetic vortices in type-II superconductors. This thesis presents intensive numerical ground state studies of systems consisting of many directed polymers with a special focus on their geometrical properties. While the ground state properties of the random field Ising model are already rather well known it serves as an ideal test problem for the quantum annealing which performance is analyzed based on the numerical calculations in one, two and three dimensions. The summary of central results and a brief discussion for both of the models are given in Chapter 4.

Chapter 2

Elastic lines in random media

In the terms of energy landscapes one could think again a hilly terrain through which one should find a path such that it follows the valleys as much as possible (high up its windy and cold) but on the other hand it should not have sharp turns or altitude changes (so it would be safe to ride a bike too). In a variety of physically relevant systems one encounters a similar set up which results to the formation of essentially line-like elastic objects. The statistical properties of these elastic lines present interesting and useful information about the underlying systems.

2.1 Single elastic line – directed polymer

2.1.1 Basic concepts

First, consider a single elastic line [7], a single magnetic flux line in a dirty type-II superconductor, for instance. The physics of such lines in most cases is encaptured in their elastic and *pinning* energy. The pinning energy describes how the line is coupled to its environment which can be usually taken to be described by a random potential. With these two ingredients in the continuum description one gets the following Hamiltonian:

$$\mathcal{H}_{single\ line} = \int_0^H dz \Big\{ \frac{\gamma}{2} \left[\frac{d\boldsymbol{r}}{dz} \right]^2 + V_r[\boldsymbol{r}(z), z] \Big\} , \tag{2.1}$$

where γ is the line tension and V_r is the random potential. In this Hamiltonian the configuration of an elastic line is described by the transverse coordinate $\boldsymbol{r}(z)$ as a function of the longitudinal coordinate z (see Fig. 2.1). This parameterization excludes overhangs which, however, are shown to be irrelevant [8, 9]. This Hamiltonian leads typically to an almost straight line which fluctuates in direction perpendicular to its preferred direction. This is illustrated in Fig. 2.1. Due to the directed nature of these objects they are called *directed polymers*.

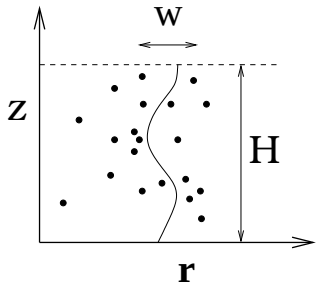

Figure 2.1: An elastic line of height H with roughness w (see Sec. 2.1.3). The random potential, which often represents localized pinning centers, is illustrated with dots.

2.1.2 Lattice formulation

In the lattice version of Eq.(2.1) the lines correspond to directed paths on a regular lattice starting from a specific lattice site and proceed only in "forward" direction. For concreteness one could consider two dimensional tilted square lattice (see Fig. 2.2) where the line starts from the corner on the bottom and can proceed only by taking steps to up-right or up-left.

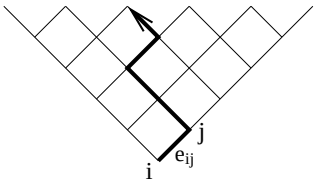

Figure 2.2: A directed polymer (bold line) on the tilted square lattice.

To the each bond of the lattice is assigned a random variable e_{ij} – the energy cost of bond (i, j). The lattice Hamiltonian is now simply the sum over

energy costs of those bonds which belong to the path:

$$\mathcal{H} = \sum_{(i,j)\in path} e_{ij} \ . \tag{2.2}$$

The ground state configuration thus corresponds to the globally lowest energy path through the lattice. The elastic term of Eq.(2.1) is now taken into account by the requirement that that within the directed path each step in the forward direction moves only one step in transverse direction. For instance on the tilted square lattice this requirement is satisfied automatically. In the case of regular lattices the optimal path can be easily found by the means of *transfer matrix* method [10].

Alternatively the shortest path can be found by using so called Dijkstra's algorithm [11] which can be successfully applied also in the case of non-regular lattices with no restrictions to the geometry of the underlying graphs. The only draw-back is the requirement of positivity of the energy costs which on the other hand automatically takes care of the elasticity requirement. The positivity of all energy costs by itself gives rise to an effective line tension. Figure 2.3 shows the optimal paths found by Dijkstra's algorithm through the square lattice from each point at $z = 0$ level of the square lattice.

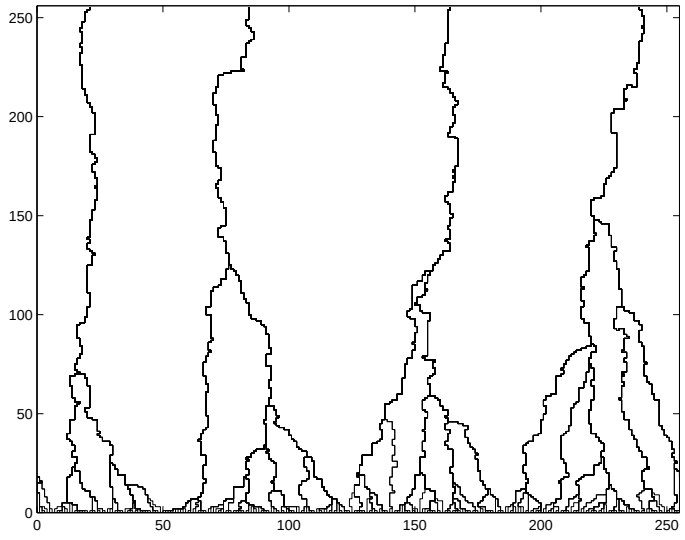

Figure 2.3: Lowest energy paths from each point at the bottom to the top of the square lattice of size 256×256 for the same realization of randomness.

2.1.3 Scaling relations

In the standard analysis of directed polymers one is interested in the fluctuations of the transverse position and of the energy of the directed polymer. Spatial fluctuations of the polymer can be described by the disorder averaged line *roughness*. The mean square displacement of a single line in one sample is defined as

$$w^2 = \overline{r^2} - \overline{r}^2 \tag{2.3}$$

with $\overline{r^n} = H^{-1} \sum_{z=1}^{H} r^n(z)$ for $n = 1, 2$. The roughness w is defined as the square root of the disorder averaged mean square displacement $w = \sqrt{\langle w^2 \rangle}$. Correspondingly, energy fluctuations δE are defined to be the standard deviation of energy over the realizations of disorder

$$\delta E^2 = \langle E^2 \rangle - \langle E \rangle^2 \,, \tag{2.4}$$

where E is the energy of a single line and brackets stand for disorder averages. The following scaling relations hold for systems consisting of single polymers in random media:

$$w \sim H^{\zeta} \tag{2.5}$$

$$\delta E \sim H^{\omega} \,, \tag{2.6}$$

where H describes the height of the sample as illustrated in Fig. 2.1. The existence of such scaling relations indicates that directed polymers are *self-affine* objects [12], i.e. they look same on the all length scales after they are rescaled according to Eq.(2.5). For the random walker the exponents are $\zeta_{RW} = 1/2$ and $\omega_{RW} = 0$ whereas for directed polymers one gets faster growing fluctuations. In the two-dimensional case the exact values of the scaling exponents are known, roughness exponent $\zeta_{2d} = 2/3$ and energy fluctuation exponent $\omega_{2d} = 1/3$ [13]. In three dimensions the exponents are obtained numerically: $\zeta_{3d} \approx 0.625$ and $\omega_{3d} \approx 0.25$ [14–17]. These two exponents, ζ and ω, are not independent but are connected with the following relation $\theta = 2\zeta - 1$ [18, 19].

Also the corresponding probability distributions $P(w, H)$ and $P(E, H)$ should scale with the exponents given above which was first checked numerically for two dimensional systems [20]. According to Refs. [20–22] $P(w) \sim exp(-(w/H^{2/3})^{\rho})$ is symmetric but not Gaussian with $\rho > 2$ whereas $P(E)$ is an asymmetric distribution with stretched exponential tails [23, 24]. In higher dimensions one expects similar results which has been confirmed for $P(E)$ [23, 25].

2.1.4 Connection to other models

Random bond Ising model

The most straightforward connection can be made to the *random bond Ising model* where the spins s are connected with random, positive coupling constants J_{ij} [18]:

$$\mathcal{H} = -\sum_{\langle i,j \rangle} J_{ij} s_i s_j \ . \tag{2.7}$$

At zero temperature due to the positivity of the coupling constants the spins want to be aligned. If the spins are forced to be "up" ($s = 1$) on the one edge of the sample and "down" ($s = -1$) on the other end, there must be a domain wall between these two edges. At zero temperature domain wall is formed such that the sum over bonds with spins of opposite orientation is minimized. Hence, in two dimensions it is nothing but the minimum energy path, that is a directed polymer.

Stochastic surface growth

The kinetic roughening of surfaces obeys the equation (2.1) as well since it can be derived from the so called KPZ equation which describes the stochastic surface growth [7, 26, 27]

$$\frac{\partial h}{\partial t} = \gamma \nabla^2 h + \frac{\lambda}{2} (\nabla h)^2 + \eta(\boldsymbol{x}, t) \tag{2.8}$$

where $h(\boldsymbol{x}, t)$ is the surface's position, $\boldsymbol{x}$ is a coordinate in the $(d-1)$-dimensional base space, η is the time and space-dependent stochastic noise and γ is the surface tension. The relation to the systems of non-interacting directed polymers is the following. The longitudinal coordinate z corresponds to time in surface growth problems. Since the directed polymer is a path that gives globally minimum energy path through the system, the polymer of longitudinal length H represents the path of the surface evolution to its highest point at a given time $t = H$.

Magnetic flux lines in type-II superconductors

Perhaps the most important and intriguing connection [28] to the real world phenomena comes from the field of superconductivity. In type-II supercon-

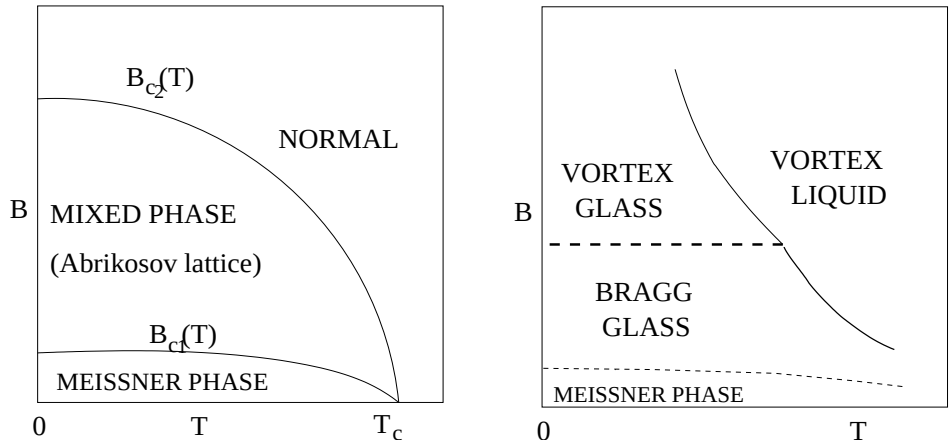

(a) (b)

Figure 2.4: (a) Mean-field phase diagram for type-II superconductors. (b) Due to disorder Abrikosov lattice is destroyed and the mixed phase splits into several sub-phases.

ductors the external magnetic field can penetrate the superconducting sample in the form of magnetic flux lines (vortices) which interact with disorder and among themselves. This leads to interesting phenomenological properties of type-II superconductors [29]. From the practical point of view it is useful to emphasize that many high-T_c superconductors are of type II.

In the mean field picture type-II superconductors are characterized by two critical magnetic fields B_{c1} and B_{c2} (Fig. 2.4(a)). When the magnetic field $B < B_{c1}$ the superconductor is in a Meissner phase. When the magnetic field B exceeds B_{c1}, the magnetic field partially penetrates the superconductor in the form of vortices each of which carries one flux quantum $\phi_0 = hc/2e$. In this, so called, mixed or Shubnikov phase in the absence of disorder flux lines form a two-dimensional triangular lattice known as the Abrikosov lattice. With increasing field the density of flux lines increases until the vortex cores overlap when the critical field B_{c2} is reached. Beyond this field the superconductivity is lost.

When an external current density j is applied to the vortex system, the flux lines start to move under the action of the Lorentz force. The movement of flux lines causes dissipation in the system and the superconducting property of dissipation-free current flow is lost. Fortunately, flux lines can be pinned by a static disorder up the critical de-pinning current density. At low tem-

perature the pinned flux lines form the vortex glass phase [30, 31], which is superconducting (or has at least an extremely small resistivity) and in which the Abrikosov flux line lattice is destroyed as in the non-superconducting vortex liquid state. At weaker disorder or at smaller magnetic fields a transition to a Bragg glass [32–34], in which the positions of the flux lines show quasi-long-range order, takes place. This has been observed experimentally [35–38] and in simulations [39]. In contrast to this (quasi)-ordered solid, the lines in the vortex glass phase are expected to be strongly entangled [40, 41]. The corresponding phase diagram is sketched in Fig. 2.4(b).

2.2 Multiple interacting elastic lines

In the case of a N-line system one has to take into account also the inter-line interaction potential V_{int}. Now, the equation (2.1) is modified to

$$\mathcal{H} = \sum_{i=1}^{N} \int_0^H dz \Big\{ \frac{\gamma}{2} \left[\frac{d\mathbf{r}_i}{dz} \right]^2 + V_r[\mathbf{r}_i(z), z] + \sum_{j(\neq i)} V_{\rm int}[\mathbf{r}_i(z) - \mathbf{r}_j(z)] \Big\} \,, \quad (2.9)$$

where the first summation goes over all lines and the second over all line pairs. The interaction term gives a rise of collective behavior which can not be described by a single line belonging to the directed polymer universality class. Thus, in the case of many line systems it is more appropriate to refer simply to elastic lines instead of directed polymers.

Usually, the studies of many line systems are described by an elastic theory [42–45] which is based on the assumption of weak disorder and low line density that is correct for the Bragg glass [32–34]. Perturbative approaches that start from a ground state with long range order and assume small fluctuations turn out to be inappropriate in a strongly disordered situation and one has to rely on numerical calculations to study the low temperature properties.

Interaction potential of flux lines has a form of the modified Bessel function $V_{\rm int}(r) \sim K_0(r/\lambda)$ which decays exponentially $K_0(x) \sim x^{-1/2}\mathrm{e}^{-x}$ for $x \to \infty$. Thus, in the case of strong screening ($\lambda \approx 0$) $V_{\rm int}$ can be approximated with hard core repulsive potential. Within this approximation it is possible to calculate the exact ground state configurations of many line systems. However, even in this approximation the ground state of many lines does not reduce to the problem of many independent lines as shown in Publication I. The

numerical method that is applied in this thesis for calculating the many line ground state is described in the next section.

2.2.1 Computing exact ground states

The ground state of many hard-core repulsive lines corresponds to N non-overlapping directed paths traversing the graph along the bonds from one side to another. One has to minimize the total energy of the whole set of the paths and not of each path individually. If this problem is approached from the perspective of the transfer matrix method one ends up to the enumeration of all possible configurations, which proliferate rapidly with the number of inserted lines.

This optimization task is convenient to formulate as an integer valued flow problem, more precisely as the *minimum-cost-flow* problem [1, 46]. Similarly to the single line case the random media is modeled with a graph to the bonds of which are assigned positive (random) energy costs. In addition, each bond represents a "pipe" which can carry one unit of flow in both directions. Since each bond can carry only one unit of flow one can distinguish N separate flow lines when N units of flow is pushed through the graph from the source node s to the target node t (see Fig. 2.5). This should be made so that the total energy of bonds that are occupied by flow is minimized. The corresponding Hamiltonian can be written as following:

$$\mathcal{H} = \sum_{(ij)} e_{ij} x_{ij} \ , \tag{2.10}$$

where e_{ij} indicates the energy cost of the given bond as in Eq. 2.2 and variables $x_{ij} \in \{0, 1\}$ determine the flow configuration, $x_{ij} = 1$ indicating that one unit of flow is going along bond (i, j), and $x_{ij} = 0$ indicating that no flow is going through this bond. Note, that now in Eq.(2.10) the summation goes over all bonds.

The optimal configuration of N flow lines can be find by applying Dijkstra's algorithm successively on a residual graph instead of the original graph as illustrated in Fig. 2.5. In the residual graph the properties of occupied bonds are modified as follows: If $x_{ij} = 1$ we set $e_{ij}^{\text{res}} = -e_{ij}$, i.e. negative, and require that the direction of a new flow path must be in the opposite direction with respect to the direction of previously inserted flow lines. If $x_{ij} = 0$ the properties of the bond are not altered and $e_{ij}^{\text{res}} = e_{ij}$. An example of the

resulting graph is shown in Fig. 2.5(b). Now, one has to find the shortest path through this residual graph. After a new path is successfully inserted to the residual graph one has to cancel the flow on the bonds where the flow is going in two opposite directions.

Since Dijkstra's algorithm works only with positive costs, introducing the negative costs to the residual graph must be taken care of. The positivity of the costs is ensured by rescaling the residual energies with the potentials (defined below):

$$e_{ij}^{\pi} = e_{ij}^{\mathrm{res}} + \pi(i) - \pi(j) \; . \tag{2.11}$$

Now, Dijkstra's algorithm is applied to the residual graph with costs e_{ij}^{π}. Potentials are calculated iteratively as follows:

$$\pi^{N+1}(i) = \pi^{N}(i) + d^{N}(i) - d^{N}(t) \; , \tag{2.12}$$

where $d^N(t)$ and $d^N(i)$ are the shortest distances from the source s to the target node t and to node i in the residual graph with positive energy costs e_{ij}^{π}. The upper indices $N+1$ and N refers to the number of lines that are

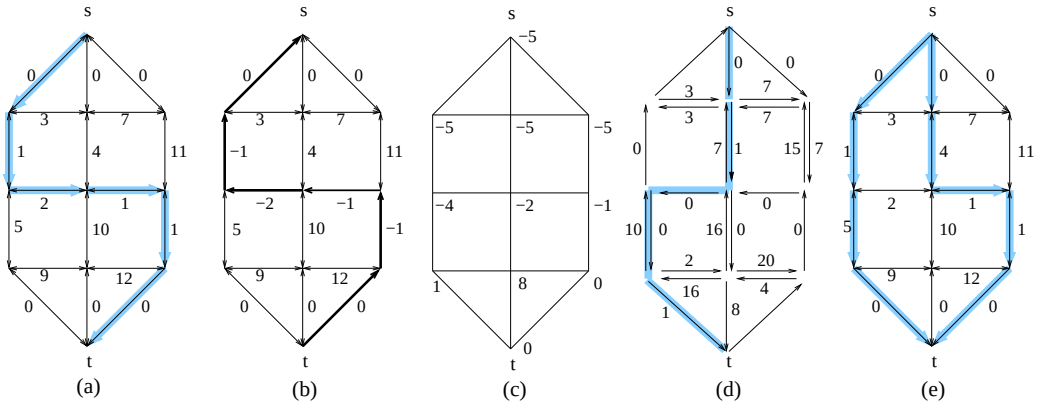

Figure 2.5: Schematic figure of adding lines to the graph. (a) The ground state of a single line with arrows indicating the direction of the optimal path with $d(t) = 5$. (b) The residual graph with modified energy costs e_{ij}^{res}. In addition, the direction of paths in the residual graph has to be opposite to the direction of the previously inserted path as emphasized with the bold arrows. (c) Node potentials $\pi(i) = d(i) - d(t)$. (d) The residual graph with positive residual costs e_{ij}^{π}, small arrows indicate the allowed path directions. The bold line marks the shortest path from s to t. (e) The final line configuration after the path segments with opposite directions are canceled.

already inserted to the graph. In the beginning of the iteration all potentials are set to zero. Whether or not to include $d(t)$ to the definition of $\pi(i)$ is a matter of taste, it just rescales the potential of the target node to zero.

Now, one has to show that the residual graph with positive costs e_{ij}^{π} gives the optimal solution as well. The residual graph with costs e_{ij}^{res} corresponds to the optimal solution if and only if there is no directed cycle $\mathcal{C}$ such that the sum of residual energies e_{ij}^{res} along $\mathcal{C}$ following only the allowed bond directions is negative (see Fig. 2.5(b)) [1]. From the definition (2.11) it follows that for any directed cycle $\mathcal{C}$:

$$\sum_{(i,j)\in\mathcal{C}} e_{ij}^{\pi} = \sum_{(i,j)\in\mathcal{C}} e_{ij}^{\mathrm{res}} \ . \tag{2.13}$$

Since the potentials are defined such that $e_{ij}^{\pi} \geq 0$ there are no negative cycles and the residual graph corresponds to the optimal solution. Thus, the optimal solution is found also with the use of potentials π as illustrated in Fig. 2.5. A more detailed proof of the optimality one can find in Ref. [1].

The augmentation of one flow line requires the search of the shortest path through the residual network which for sparse graphs with Dijkstra's algorithm can be roughly done with the complexity of $O(|A|)$, where A is the set of the bonds [11]. So, the total complexity is $O(N|A|)$ where N is the number of inserted lines. The program implemented for the calculations that are overviewed in this thesis has been found to scale like $O(NL^{2.2})$ for the square graphs and for the cubic graphs $O(NL^{3.4})$ where L is the linear size of the graph.

2.3 Point disorder

2.3.1 Separability of the ground state

As the first approximation to the ground state configuration of many repulsive elastic lines one can consider the following construction. Lines are inserted to the system independently such that each line corresponds to the optimal path in the graph where the bonds occupied by previously inserted lines are erased. It is obvious that as the density of lines grows this approximative method fails excessively as illustrated in Fig. 2.6.

It turns out that already the problem of two lines is not separable (Publication I). This is tested in the square and cubic lattices where two lines start

next to each other at the basal plane ($z = 0$) but have arbitrary endpoints at the top of the system ($z = H$). In order to avoid any boundary effects the width of the systems is equal to their height: $L = H$. The separability is measured in terms of effective interaction energy of two lines for which it is defined as the energy difference between the true ground state of two lines E_2 and the state obtained by using the approximative construction described above E_2' :

$$V_{int} = E_2' - E_2 = E_1 + E_1' - E_2 \ , \tag{2.14}$$

where E_1 is the ground state energy of a single line system and E_1' is the energy of the first excited state (the second line in the approximation). The interaction energy can be described also as:

$$E_{int} = E_2 - 2E_1 \ , \tag{2.15}$$

following the definition given in Ref. [47] which provided the first numerical results concerning the systems of two hard-core repulsive lines. Disorder averages of these interaction energies are expected to scale with a power law as a function of system size L:

$$V_{int} \sim L^{\theta_V} \ , \qquad E_{int} \sim L^{\theta_E} \ , \tag{2.16}$$

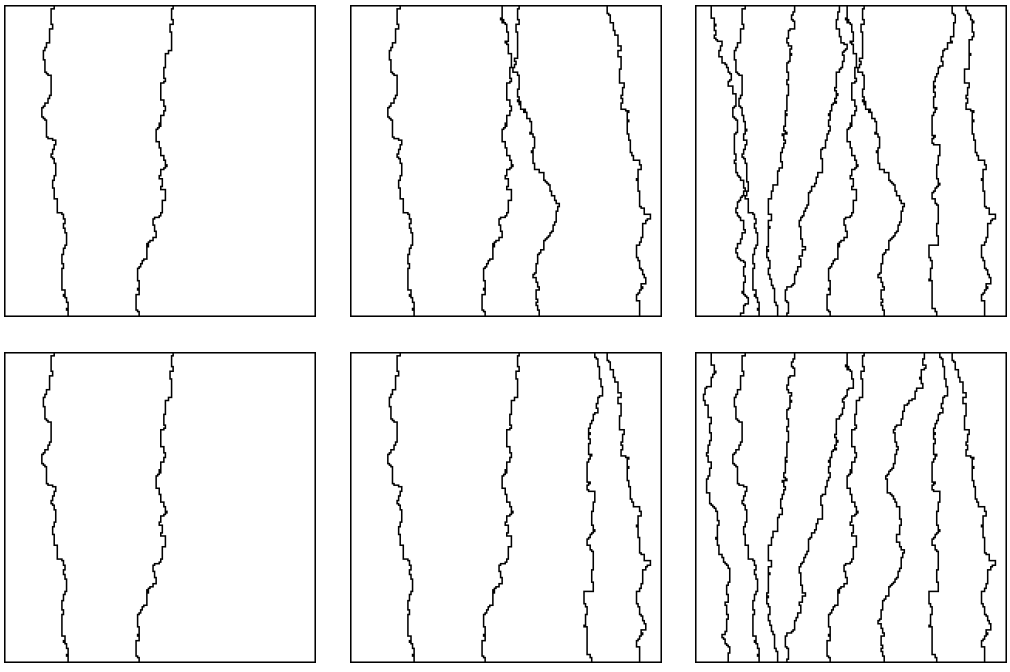

Figure 2.6: Top: true ground states. Bottom: separate single lines with increasing energy.

with the exponents θ_V and θ_E defining the scaling of the effective interaction energies. Positivity of θ_V and θ_E would automatically imply that the ground state of two lines is not separable which is clearly demonstrated in Fig. 2.7.

Recall that the energy fluctuation exponents for a single line are $\omega_{2d} = 1/3$ and $\omega_{3d} \approx 0.25$ in two and three dimensions respectively. The earlier results on two dimensional systems [47–49] suggest that the interaction energy between two lines should grow like $L^{\omega_{2d}}$. The numerical data presented in Fig. 2.7 strongly supports this scenario, and it seems to hold also in three dimensions. Thus one can conclude that:

$$\theta_E = \theta_V = \omega \ . \tag{2.17}$$

More details are presented in Publication I. As a follow-up to this analysis one could consider the separability of the systems with finite line densities. Also the studies of topological properties of the overlap between the ground state and the excited states could give some new information concerning the unpinning mechanisms of magnetic flux lines.

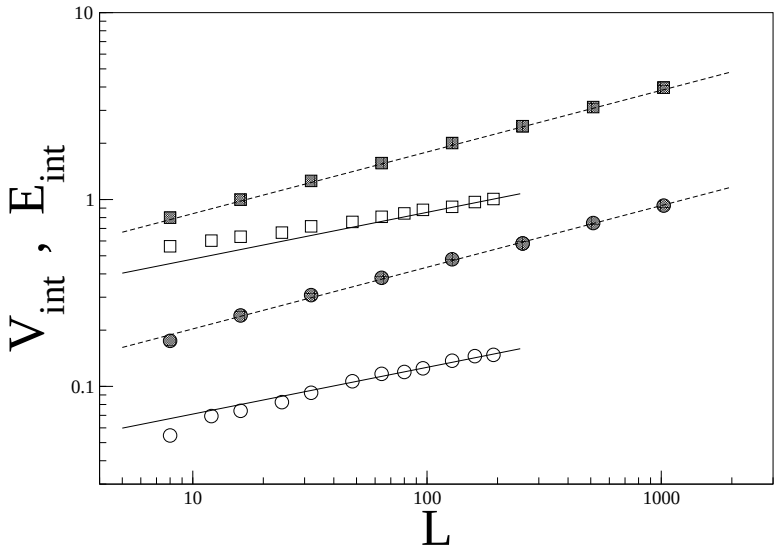

Figure 2.7: Doubly logarithmic plot of the effective interaction energies V_{int} (ovals) and E_{int} (squares) as a function of system size L for the square (filled symbols) and cubic lattices (open symbols) with uniformly distributed energy costs. The straight lines are guides for an eye, full lines with slope 0.25 and dashed lines with slope 0.33.

2.3.2 Roughening

The geometrical properties of single line systems are rather well understood as described in Sec. 2.1 but the effects of the collective behavior on the roughening of lines need some clarification. It is interesting to know whether the elastic theories [45], which are limited for long range interactions, weak disorder and low line-densities, give the correct behavior in a strong disorder, short range interaction limit.

In two dimensions elastic manifolds exhibit a *super-rough* behavior with logarithmically diverging displacements. This was shown analytically for the surfaces of crystals with quenched bulk disorder where the fluctuations of the interface position diverge like $\log L$ as the length of the surface $L \to \infty$ [50]. This scaling is also obtained with numerical calculations [51]. As a starting point for the analysis in 3d is usually an ordered lattice of lines. In the elastic approximation one assumes that the displacement (from the lattice) of a line is varying slowly on the scale of the lattice. In this description the difference between the displacements separated by distance L grows like $\sqrt{\log L}$ [33, 42–44]. Simulations, where the 3d elastic manifold is represented by an interface in a $(3+1)$-dimensional system, agree with this analytical result [52].

In the numerical work presented in Publication II the roughness is calculated for N lines which are confined in a box of width L and height H. First, the squared roughness w^2 is calculated for the each line individually according to the definition given in Eq.(2.3). w^2 is averaged over the all lines of a given sample, which is then subsequently averaged over the randomness. The number of lines threading the sample is fixed by a prescribed density ρ which is defined as $\rho = N/L$ and $\rho = N/L^2$ in two and three dimensions, respectively.

In the case of a non-vanishing line density one expects to observe the single line behavior (see Sec. 2.1.3) as long as the transverse fluctuations of the individual lines are smaller than the average line-to-line distance a, which is given by the line density $\rho = 1/a$ in two dimensions and $\rho = 1/a^2$ in three dimensions. This means that one can expect $w \sim H^{\zeta}$ for $H \ll a^{1/\zeta}$ which is also confirmed by numerical results both in two and three dimensions, whereas the collective behavior turned out to be totally different.

Two dimensions

Once the transverse fluctuations of the individual lines have reached the size of average line-to-line distance one expects a collective behavior of the lines that restricts the individual line roughness due to the presence of the others. If the line system behaves like an elastic medium the roughness in the collective regime is expected to behave like $w \sim \log L$ [50, 51]. According to the data collapse of the numerical data shown in Fig. 2.8 for fixed line density ρ the roughness has the two following scaling regimes:

$$w \sim \begin{cases} H^{\zeta}, & (H \ll a^{1/\zeta}) \\ \log L, & (H \gg a^{1/\zeta}) \end{cases} \tag{2.18}$$

This means that in the collective regime the elastic description is valid even if the lines have just a hard core repulsion.

Line density enters to the scaling properties simply considering the the crossover from single-line to multi-line scaling which takes place when $H^{\zeta} \sim a$. For fixed but large lateral system size L the scaling form (2.18) predicts

$$w \approx a \cdot g_{2d}(H/a^{1/\zeta}) \tag{2.19}$$

where the scaling function $g_{2d}(x)$ has the asymptotic behaviors $g_{2d}(x) \sim x^{\zeta}$ for $x \ll 1$ and $g_{2d}(x) \sim const.$ for $x \gg 1$. This is also confirmed with the numerical results shown in Publication II.

Three dimensions

On the basis of extensive numerical calculations presented in Publication II one can distinguish in three dimensions the following three scaling regimes:

$$w \sim \begin{cases} H^{\zeta}, & (H \ll a^{1/\zeta}) \\ H^{1/2}, & (a^{1/\zeta} \ll H \ll L^2) \\ L, & (L^2 \ll H) \end{cases} \tag{2.20}$$

While in two dimensions the scaling of the single line regime continuously crosses over to the stage of saturation as H is increased, in three dimensions one has an intermediate regime where the roughness has a random walk like scaling $w \sim H^{1/2}$. Further, according to the elastic theory one would have expected that the roughness in the collective regime would scale like $w \sim$

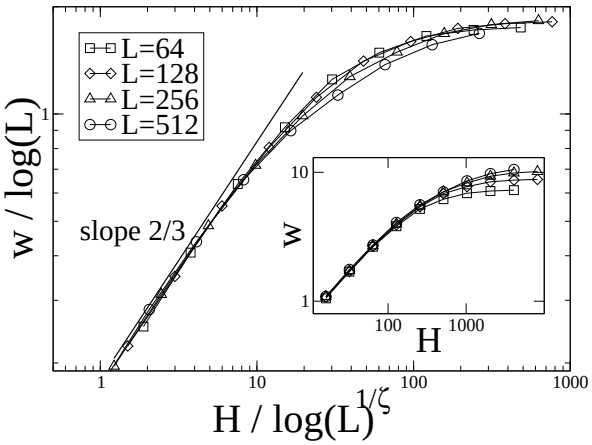

Figure 2.8: Scaling plot of the roughness in 2d with the line density $\rho = 0.05$ according to Eq.(2.18) with the roughness exponent $\zeta = 2/3$.

$\sqrt{\log L}$ [33, 42–44, 52]. Instead, we observe a linear growth of the saturation roughness $w_{H\to\infty} \sim L$.

These properties of the collective behavior can be explained as a consequence of the fact that in three dimensions lines can bend around each other which diminishes the effects of the steric repulsion. One can visualize this result also by looking at the disorder averaged position of the center of mass of the individual lines (which is $\overline{r}$ as defined below Eq.(2.3)). In 2d they constitute a regular array with lattice spacing a when the entrance points of lines are fixed at $z = 0$ in each sample to the same positions with spacing a. In 3d, as it is shown in Fig. 2.10, they still constitute a regular array, but it concentrates, with increasing height, more and more in the central region of the basal plane of the system. In the limit $H \to \infty$ the average center of mass position of each individual line will be exactly at the center of the system since nothing restricts it from traversing the system from the one side to the other.

Eq.(2.20) defines two cross-overs density dependencies of which have to be treated separately. The first cross-over corresponds the change from the single- to multi-line regime. Here the relevant length scale in the H-direction is $a^{1/\zeta}$, and in analogy to the 2d case we expect for $L \gg a$ the L-independent scaling form

$$w = a \cdot g_{3d}(H/a^{1/\zeta}) \tag{2.21}$$

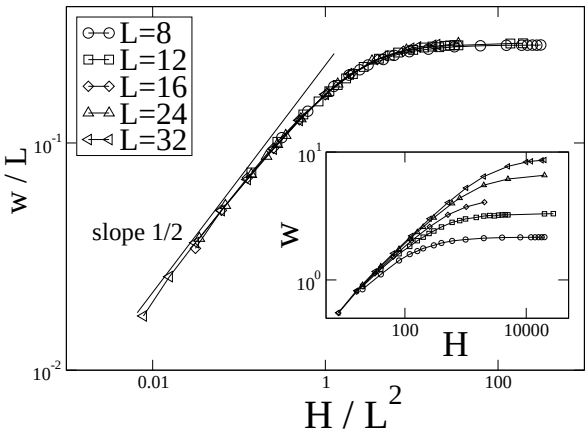

Figure 2.9: Scaling plot for the roughness in 3d with the line density $\rho = 0.2$ for the transition from the collective regime to the saturation roughness.

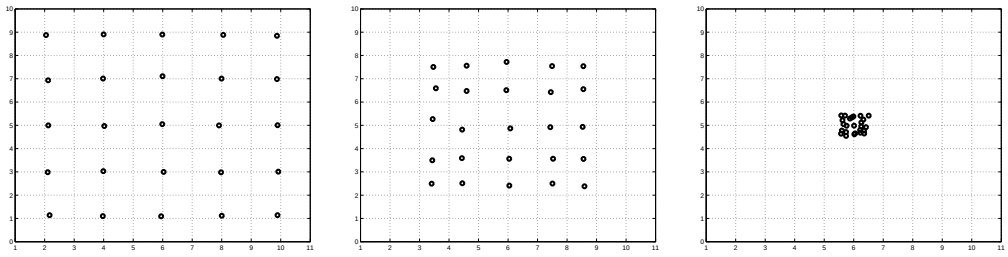

Figure 2.10: Average positions of center of masses of lines with fixed starting points. From left: H=10, H=100, H=1000. Note that the center of mass position is averaged over the disorder, here 1000 samples.

with the asymptotics $g_{3d}(x) = x^{\zeta}$ for $x \ll 1$ and $g_{3d}(x) = x^{1/2}$ for $x \gg 1$. Hence we get the expected single line behavior $w \sim H^{\zeta}$ when $H \ll a^{1/\zeta}$, and for the collective regime, where $w \ll L$ and $H \gg a^{1/\zeta}$, one obtains

$$w = a^{1-(1/2\zeta)} H^{1/2} = (H/a^{1/\zeta-2})^{1/2} \, . \tag{2.22}$$

From this one can conclude that the cross-over from the intermediate regime to the saturation regime takes place at $H \sim a^{1/\zeta-2} L^2$. The corresponding data collapses can be found in Publication II.

2.3.3 Entanglement

In 2d it was sufficient to measure the roughness of lines in order to get a rather complete picture about the geometrical properties of the system. This is not the case in three dimensions. Due to the increased dimensionality of the system lines can bend around each other resulting in complicated configurations of entangled lines.

The existence of entangled state due to thermal flux-line wandering was first discussed in Ref. [53], and shortly after that also the disorder-induced entanglement was considered [28]. The topological entanglement of the magnetic flux lines in high-T_c superconductors is believed to enhance the critical current [40, 54]. Thus, the understanding this topologically highly non-trivial state, including the the conditions under which it occurs, is highly desirable. For a single line the entanglement has been measured in terms of winding angle ϕ [41, 55] which in point disorder is found to grow like $\phi \sim \sqrt{\log H}$. In the thermal case the result for the winding of a random walk is $\phi \sim \log H$ [56, 57]. For the analytical studies of the collective entanglement there has been proposed a random braiding model [58] which was used for computing characteristic disentanglement times. To our knowledge there have not been reported any other results from this model.

In this thesis the entanglement of lines is analyzed by computing the winding angle of all line pairs as indicated in Fig. 2.11(a). We define two lines to be *entangled* when the winding angle becomes larger than 2π. This measures entanglement from the topological perspective [41, 58], arising from the requirement that an entangled pair of lines can not be separated by a suitable linear transformation in the basal plane (ie. the lines almost always would cut each other, if one were shifted).

Sets or *bundles* of pairwise entangled lines are formed so that a line belongs to a bundle if it is entangled at least with one other line in the set. In the case of point disorder such bundles are spaghetti-like — i.e. topologically complicated and knotted sets of one-dimensional objects which grow with increasing system height leading finally to one giant bundle. The structure of the resulting bundles, or cluster, is illustrated in Fig. 2.11(b) which shows the 2d projection of a typical multi-line system. For clarity, only the mass centers of the lines are shown (ovals). There is a link between two mass centers if the lines are entangled. The resulting clusters grow and merge as the system hight H is further increased.

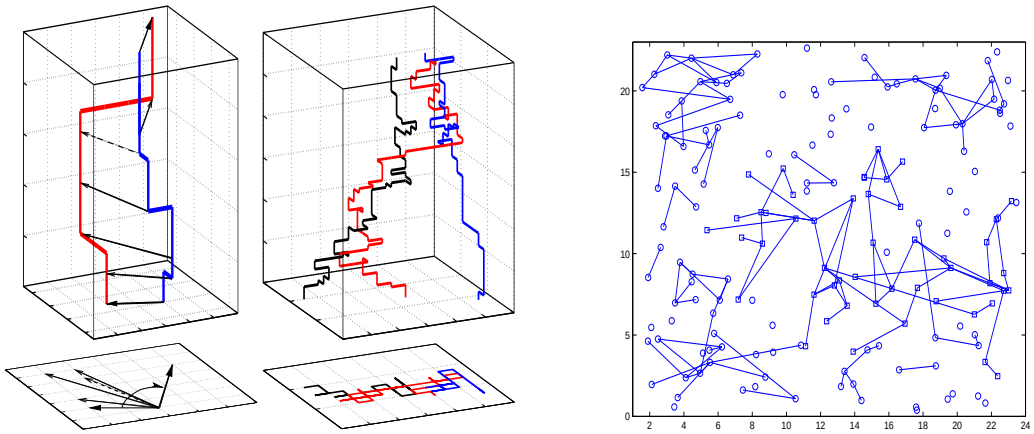

(a) (b)

Figure 2.11: (a) Left: Definition of the winding angle of two flux lines: For each z-coordinate the vector connecting the two lines is projected onto that basal plane. The vector at $z = 0$ is the reference line with respect to which the consecutive vectors for increasing z-coordinate have an angle $\phi(z)$. Once $\phi(z) > 2\pi$ the two lines are said to be entangled. Right: A configuration of three lines that are entangled. (b) L=24 H=120 $\rho = 0.3$, mass centers of lines, entangled lines connected.

In Fig. 2.12 is shown the probability P_{perc} of the clusters of entangled bundles to percolate as a function of the height H of the system. The curves for different lateral system sizes L intersect at H_c, which gives our estimate for $H_c(\rho = 0.3) = 134$. The inset shows a scaling plot according to

$$P_{\text{perc}} = p\left(L^{1/\nu}(H - H_c)/H_c\right) \tag{2.23}$$

with $\nu = 4/3$ which is the exponent of conventional bond percolation in two dimensions. Thus, one can conclude that the transition is in the universality class of conventional $2d$ percolation. This result is confirmed by considering other quantities such as the bundle size distribution and the fractal dimension of the bundle at the criticality (Publication III). Also the density ρ can be used as a control parameter giving similar results for the transition.

This result corresponding to the 2d percolation problem is somewhat surprising, since one could expect the entanglement of two lines to have correlations. These, if long ranged, change the percolation universality class [59]. Why this is not true is seen from the probability for two lines with mass center distance r to be entangled, $P_{\phi>2\pi}(r)$ (Fig. 2.13). It decays exponentially

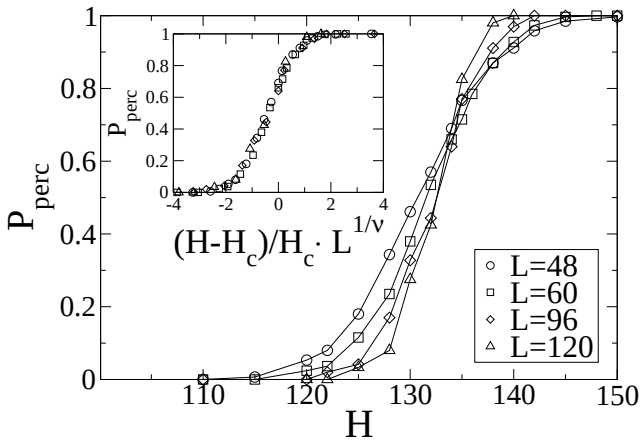

Figure 2.12: Percolation probability for different lateral system sizes L as a function of the system height H, the line density is $\rho = 0.3$. Inset: Scaling plot of the data with $H_c = 134$ and $\nu = 4/3$.

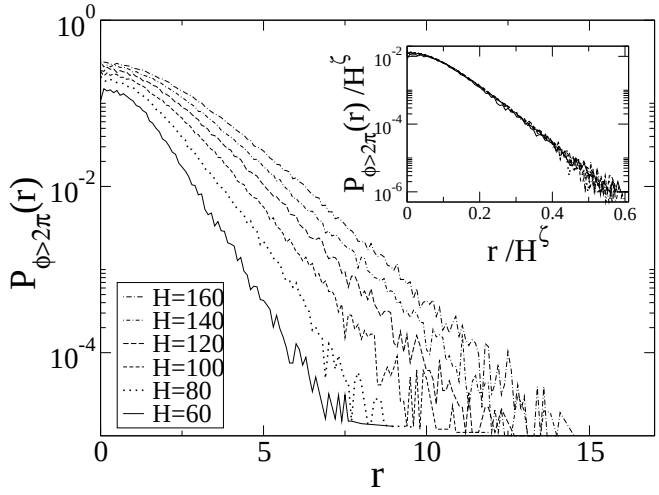

Figure 2.13: Probability $P_{\phi>2\pi}(r)$ that two lines at a mass center distance r have a winding angle larger than 2π, i.e. are entangled. Inset: Scaling plot, according to $P_{\phi>2\pi}(r) = H^{\zeta}\tilde{p}(r/H^{\zeta})$. $\zeta = 0.62$ is the single line roughness exponent. The lateral system size is $L = 60$, since $r \ll L$ there is no finite L effect.

with r, implying at least for two-line-entanglement only short range correlations. It scales with the transverse fluctuations of a single line H^{ζ}, where

$\zeta = 0.62$ is the single-line roughness exponent in 3d (see Sec. 2.1.3), so that $P_{\phi>2\pi}(r) = H^{\zeta}\tilde{p}(r/H^{\zeta})$. It is noteworthy that the "really entangled" lines follow a scaling stemming from single-line behavior. Three-line correlations (e.g. the probability of a third line to be entangled with one or two others, given that these two are entangled or not), are also only short-ranged.

It should be pointed out that thermally fluctuating lines have the same entanglement transition as discussed above. The only difference is that the data for $P_{\phi>2\pi}(r)$ collapses with the random walk exponent $\zeta_{RW} = 1/2$. This is shown numerically in Publication III.

2.4 The effects of splay disorder

It was proposed by Hwa *et al.* [60] that splayed columnar defects resulting from heavy ion irradiation of superconducting samples, would significantly enhance the vortex pinning, and thus reduce the vortex creep leading to a higher critical current density j_c. The predictions concerning j_c have been been verified in experiments on samples with different sources of splayed defects [61–63].

Kwok et al. [63] reported that well above the matching field B_ϕ, where the density of vortices equals to the density of columnar defects, the irreversibility line of sample with splay is below of the one without splay defects. As evidence of strong entanglement above the matching field it was discovered [63] that although the irreversibility is decreased in samples with splay defects values of j_c are still greatly increased compared to unirradiated samples. On the other hand the comparison of samples with one and two families of splay defects with different tilt angles did not reveal any differences in the values of j_c below B_ϕ [64]. From this result one could conclude that lines are not entangled in this particular set up.

Single flux line properties in the presence of tilted columnar defects at zero temperature were studied by Lidmar et al. [65]. They show that the roughness exponent ζ is sensitive to the shape of the tilt angle and energy distributions of the defects [65]. For instance with an opening angle of 90° and for a uniform energy distribution the roughness exponent in 2d is $\zeta = 3/4$, in contrast to the point-disorder result 2/3 [13, 18]. In samples with a fixed starting point a single line has the following geometry. It occupies a splay defect until a jump to a energetically more favorable one takes place. The

lines undergo jumps from splay defect to splay defect so that the average distance between two successive jumps grows as $\Delta z \sim z$ [65]. Though the jump density decreases with growing z the roughening exhibits a non-trivial scaling.

The natural question arises how the single-line physics outlined above changes in the presence of many interacting lines, at a constant line density ρ. On the other hand it is interesting to know how the results differ from the case of point disorder discussed earlier in this thesis.

2.4.1 Model

In principle we use the same model as in the case of point disorder, the ground state configuration is calculated with the same algorithm as described in Sec. 2.2.1. However, now the underlying graph is constructed of an ensemble of splayed columns embedded in a box with a width L and a height H (Fig. 2.14). Each column is described with a transverse coordinate $\mathbf{r}(z)$ at height z from the bottom level:

$$\mathbf{r}(z) = \mathbf{r}_0 + \mathbf{a}\, z \tag{2.24}$$

where $\mathbf{r}_0$ is a random point on the basal plane and $\mathbf{a}$ is a randomly chosen variable that defines the magnitude and the orientation of the tilt of a given column.

The number of columnar defects M is set to $M = L$ and $M = L^2$ in two and three dimensions respectively. The average distance between two nearby columnar defects defines the in-plane length unit of the model. In the case of point disorder boundary conditions on entry and exit plains do not alter the many line configurations whereas this is not so for splay disorder. The case of a fixed entry point and a free exit point is that considered by Lidmar et al. for a single line [65].

2.4.2 Roughness

In order to make comparisons to single line results by Lidmar et al. we use the following distribution for the energy costs u per unit length of the splayed defects

$$P(u) = \nu u^{\nu-1}\,, \tag{2.25}$$

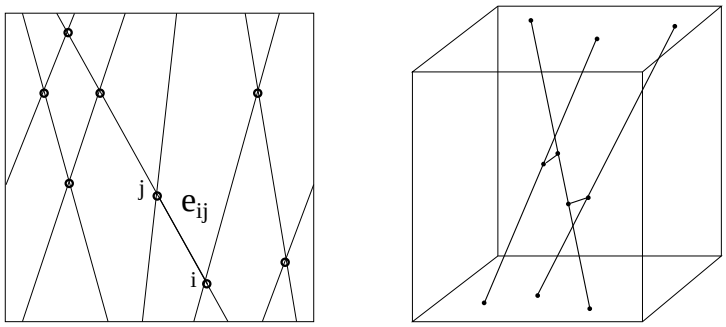

Figure 2.14: Schematic figure of the graph consisting of splayed columns in two and three dimensions. In the latter case note the two additional bonds connecting the columns.

for $0 < u < 1$ and otherwise $P(u) = 0$. With $\nu = 1$ this is a uniform distribution. The energy cost e_{ij} (see Fig. 2.14) of a particular bond is $e_{ij} = u\, r_{ij}$, where r_{ij} is the length of the bond. When the energy cost u is drawn independently (from the uniform distribution in this case) for each bond, no matter whether they are on the same splayed defect or not, one ends up to the point disordered system in which lines have the same scaling properties as discussed in Sec. 2.3. As shown in Fig. 2.15 our numerical results for single line systems are in a good agreement with those of Lidmar et al.

Figure 2.16 shows the typical line configurations for point and splay disorder. The underlying graph in the both cases is the same apart from the energy cost distributions of the bonds. In splay disorder lines change the defects relatively close to the basal plane after which they stick to one defect resulting a ballistic behavior in the collective regime. For many line systems we propose the following simple scenario. At small z lines do not see each other and exhibit single line behavior. Beyond some value of z, which depends on the density ρ, the lines cannot further optimize their configurations and stay on the same defects. This leads to a linear growth of the roughness both as a function of the width and height of the system. In 3d this scenario is confirmed with the data collapse shown in Fig. 2.17. According to the data collapse of Fig. 2.18 in 2d the collective regime has a random walk like behavior since when two neighboring occupied splay defects meet, the flux lines change defects. Thus, one gets for the crossover from the collective behavior to the saturation of roughness the following scaling form

$$w(L, H) \propto L^{\zeta} f(H/L), \tag{2.26}$$

where $f(x)$ is a scaling function and $\zeta = 1/2$ in 2d and $\zeta = 1$ in 3d. In both

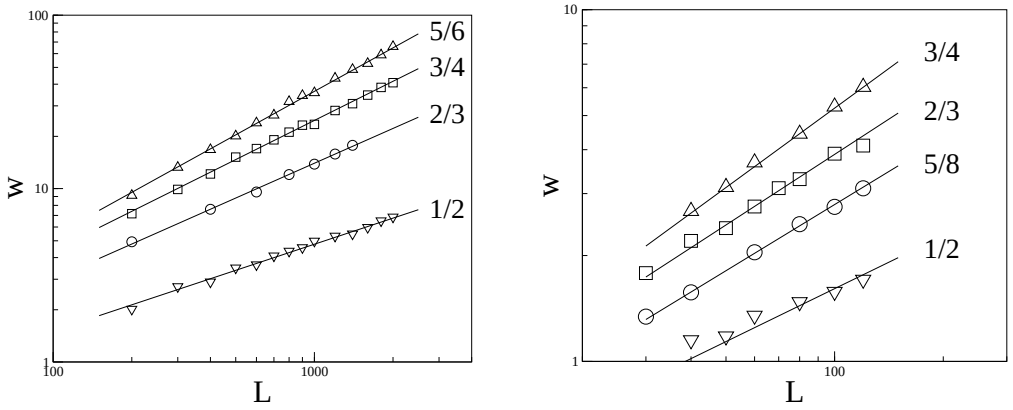

Figure 2.15: (a) A doubly logarithmic plot of single line roughness in 2d (a) and 3d (b) in systems with splay disorder corresponding to $\nu = 0$ (triangle down), $\nu = 1$ (square) and $\nu = 2$ (triangle up). For comparison also the data for point disorder (ovals) are shown. Straight lines with the expected slopes given in Ref. [65] are guides for the eye.

2d and 3d, this scenario is independent of the splay energy distribution.

It is obvious that with periodic boundary conditions and the full freedom of choosing the most favorable starting point the lines pick up the defects in the order of their total energy cost from the source to the target. Hence, no rearrangements of flux line configurations is needed. This implies that the ground state of many lines in splay disorder is *separable*. However, introducing boundaries or any other distortions to the pure columnar disorder reduces the separability of the ground state.

2.4.3 Entanglement

A priori it is not clear whether the jumping of lines close to the basal plane and in the vicinity of the system boundaries combined with the ballistic bulk behavior could enhance or diminish the total entanglement. It turns out that the boundary effects alone can not generate the entangled state in the thermodynamical limit. Similarly to the case of point disorder one can define the percolation probability P_{perc} which is shown as a function of H for several system widths L. As one can see from Fig. 2.19 H_c does not saturate for the

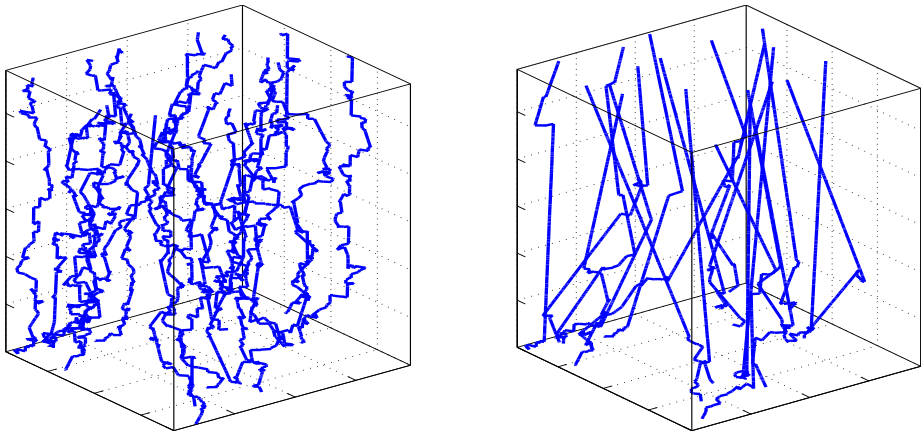

Figure 2.16: Left: a typical line configuration in point disorder. Right: splay disorder.

computationally accessible system sizes ($L \lesssim 120$). From the inset one can also see that the width of the transition does not decrease.

Detailed analysis given in Publication IV shows that in the case of splayed columnar disorder the spanning bundles are formed mostly by few lines which bounce from the boundaries of the system. Thus the percolation in splay disorder resembles the finite size effects in point disordered systems caused by single line percolation. However, the entanglement can be triggered by perturbing the pure splay system with point defects. If the perturbing point disorder is strong enough the percolation-type entanglement transition to the 2d percolation universality class is recovered.

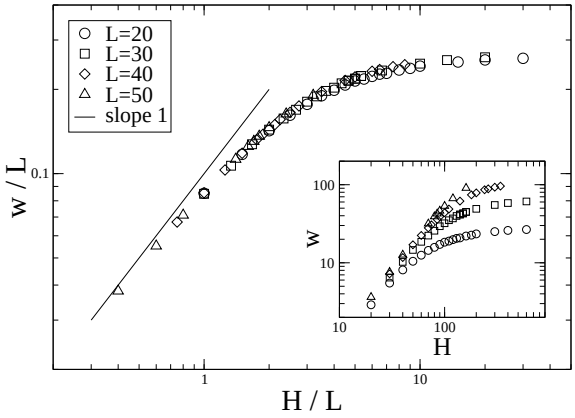

Figure 2.17: Scaling plot for the roughness in 3d for the data corresponding to $\rho = 0.2$ and $\nu = 1$. At this density (inter-line distance $a = 1/\sqrt{\rho} \approx 2.2$) the single line regime is not visible.

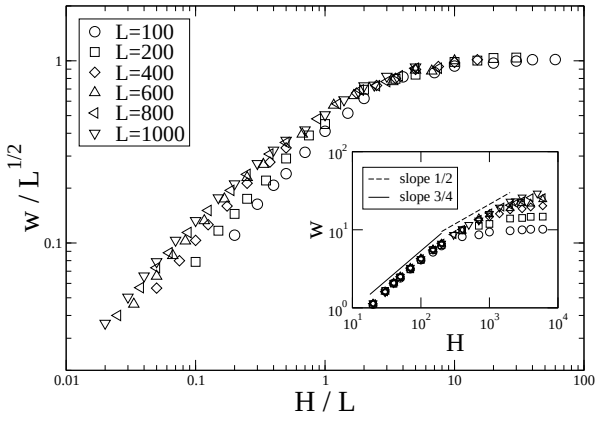

Figure 2.18: Scaling plot for the roughness in 2d for the data corresponding to $\rho = 0.1$ and $\nu = 1$. Inset: the un-scaled date, note the crossover from the single lines to the collective regime.

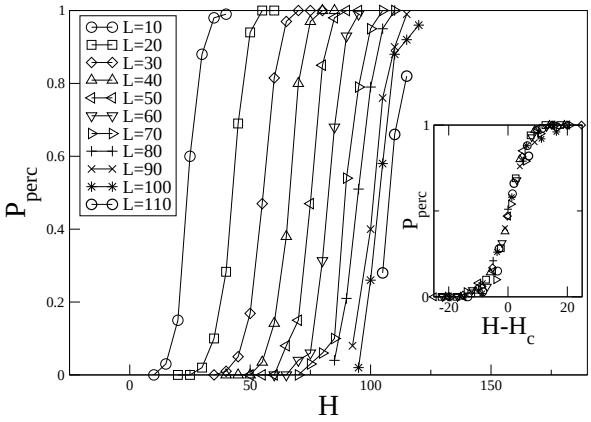

Figure 2.19: Percolation probability P_{perc} vs. system height H. Inset: the transition does not sharpen with increasing system widths, H_c is defined as $P_{perc}(H = H_c) = 0.5$.

Chapter 3

Quantum annealing

3.1 Introduction

It is desirable to have an optimization method which can be easily applied to a wide range of problems. An example of such method is the classical simulated annealing (SA) for which a convenient measure of the effectiveness is the residual energy e_{res}. It is defined as the energy difference between the true ground state and the configuration that is obtained in the end of the annealing process. Another important quantity is the annealing time τ, during which the temperature of the system is reduced to zero. When τ is increased the energy of the resulting configuration approaches the ground state energy. In the case of SA the residual energy e_{res} decreases with the annealing time τ as [5]

$$e_{res} \sim \log(\tau)^{-\zeta} \quad . \tag{3.1}$$

For large time scales the upper limit for the decay of the residual energy in two-level systems is given by $\zeta \leq 2$ [5]. This is considered as a generic result for disordered systems since in many cases they can be coarse grained to a two-level system. In some cases the annealing can be even slower. For instance, when a random field magnet is cooled through the phase boundary from the disordered to the ordered phase the annealing slows down to $\zeta = 1$ [5]. Thus, the wide applicability of SA is hindered by its un-effectiveness – logarithmically slow convergence towards the optimal solution.

A quantum annealing (QA), the quantum mechanical version of SA, turned out to be a promising method sharing the benefits of SA with a faster convergence [66, 67]. In SA the annealing process exploits thermal fluctuations

which are tuned by changing the temperature. Similarly, in QA one takes advantage of quantum fluctuations which requires that one works in the ideal case at zero temperature. In the case of spin systems quantum fluctuations can be tuned by a transverse (magnetic) field. The research of QA has been partly motivated by its real world realizations, demonstrated in experiments by Brooke et al. [68, 69]. They found that when a disordered ferromagnet is put into a strong transverse magnetic field which is then slowly reduced to zero the system relaxes faster than in the case of pure thermal annealing. Thus, it seems that by tuning the quantum fluctuations instead of thermal fluctuations the annealing process can be more efficient.

In Ref. [66] Santoro et al. have derived a theoretical estimate for the decay rate of the residual energy. They argued that the residual energy comes from tunnelings at (avoided) Landau-Zener (LZ) crossings. The corresponding average residual energy resulting from this process was estimated as $e_{res}(\tau) = \int_0^{\Gamma_0} d\Gamma\, Z(\Gamma) E_{ex}(\Gamma) \exp(\tau/\tau_c(\Gamma))$ where $Z(\Gamma)$ is the density of LZ crossings and $E_{ex}(\Gamma)$ is the corresponding average excitation energy. The term $\exp(\tau/\tau_c(\Gamma))$ gives the probability that the system tunnels during the annealing to a higher energy eigen-state due to LZ crossings, and $\tau_c(\Gamma) \sim \exp(A/\xi(\Gamma))$ where ξ is a typical wave localization length. Ref. [66] now considers the limit $\Gamma \to 0$ which is expected to dominate the annealing behavior. With the assumptions $\xi(\Gamma) \sim \Gamma^{\varphi}$ and $Z(\Gamma)E_{ex}(\Gamma) \sim \Gamma^{\omega}$ one gets $e_{res} \sim \log(\tau)^{-\zeta}$ with $\zeta = (1+\omega)/\varphi$. With the estimates $\varphi = 1/2$ and $\omega = 2$ given in Ref. [66] one gets $\zeta = 6$. The value for φ comes from a quasi-classical consideration of a particle's wave length, whereas $\omega = 2$ can be reasoned for as follows. In the limit $\Gamma \to 0$ the tranverse field can be considered as a perturbation for which only the second order correction to the energy has a non-zero value. From this follows that $E_{ex} \sim \Gamma^2$. If the density of LZ crossings in the limit $\Gamma \to 0$ is assumed to be at most the density of the classical states at $\Gamma = 0$ one gets $\omega = 2$. Thus the residual energy decreases logarithmically but now with much larger exponent $\zeta \approx 6$. This implies a considerable speed-up compared to $\zeta = 2$, the upper limit of SA. It is useful to emphasize that this estimate for ζ is obtained without any problem–specific assumptions.

The best way to see the usefulness of QA in solving optimization problems is to test its performance in practice. Test problems for QA can be found from many problem–specific optimization algorithms which find the exact ground state in a polynomial time, as for instance the random field Ising model or the Ising spin glass in two dimensions [1]. When the optimal solution is available the residual energy can be calculated straightforwardly.

The numerical results of Santoro et al. [66] show that the residual energy of the 2d Edwards-Anderson spin glass converges indeed at a much faster rate and to lower values with QA, compared to SA, though no empirical values of ζ were given. In addition, the performance of QA has been tested also on the traveling salesman problem [67] for which similarly to the 2d spin glass QA gives a faster decay of the residual energy than SA. However, this is not generally valid for all optimization problems. Battaglia et al. [70] have found that in the case of the three-satisfiability problem quantum annealing is outperformed by simulated annealing. In small systems, it is possible to see a power law decay of the residual energy $e_{res} \sim \tau^{-\alpha}$, e.g. by solving the time-dependent Schrödinger equation adiabatically [71, 72]. The exact value of α seems to depend on the underlying system and the details of the annealing. For a double well potential $\alpha = 1/3$ [72] whereas for small spin systems (N=9) $\alpha = 2$ [71], which is confirmed with the density matrix renormalization group [73] to hold also for a random Ising chain of 80 spins [74]. However, with increasing system sizes the energy gap for the Landau-Zener crossings decreases [75], which means that the probability of staying in the ground state decreases as well leading to the logarithmic behavior discussed above.

3.2 Random field Ising model

In this thesis we study the quantum annealing applied to the random field Ising model (RFIM). Its classical version has the following Hamiltonian:

$$H = -J \sum_{\langle i,j \rangle} s_i s_j - \sum_i h_i s_i \ , \tag{3.2}$$

where $J > 0$ is the coupling constant, $s_i = \pm 1$ are classical spin variables and h_i is the random field at site i. In the first term of Eq.(3.2) $\langle i, j \rangle$ denotes the summation over the nearest neighbor spin pairs. One of the advantages of RFIM as a test problem is the fact that its exact ground state can be found in a polynomial time with an efficient graph algorithm from combinatorial optimization [1].

Another advantage of RFIM is a tunability of the strength of disorder. It is well known that in the absence of the random field one has long range order in one dimension only at zero temperature whereas in two and three dimensions the system has a second order phase transition at non-zero temperature. The presence of the random field destroys the long range order in one and two

dimensions [76], also at zero temperature. However, in three dimensions one has a temperature dependent critical strength of the random field $h_c(T)$ below which the system is ordered [77, 78]. At zero temperature its value has been calculated numerically: $h_c(T = 0) = 2.27$ for Gaussian random field distribution [79]. Though there is no long range order either in one or two dimensions, systems of a finite size may have ordered ground states when the typical cluster size exceeds the system size. This finite size effect is especially emphasized in two dimensions [80, 81]. The structure of the 2d RFIM ground state is illustrated in Fig. 3.1. The values of random field h_i are taken from the fixed Gaussian distribution $P_G(h_i)$ with the parameters $\langle h_i \rangle = 0$ and $\langle h_i^2 \rangle = 1$. The strength of the random field is tuned by varying the ferromagnetic coupling J.

The quantum version of Eq. (3.2) is obtained by replacing the spin variables s_i with Pauli spin operators σ_i^z. Quantum fluctuations are tuned by changing the strength Γ of a perpendicular field term, arising from the Pauli spin operator σ_i^x.

$$H_Q = -J \sum_{\langle i,j \rangle} \sigma_i^z \sigma_j^z - \sum_i h_i \sigma_i^z - \Gamma \sum_i \sigma_i^x. \tag{3.3}$$

In the quantum annealing one starts with a large value of Γ so that spins in the z direction are totally uncorrelated. By decreasing Γ gradually towards zero spins fall into the ground state configuration provided that $T = 0$.

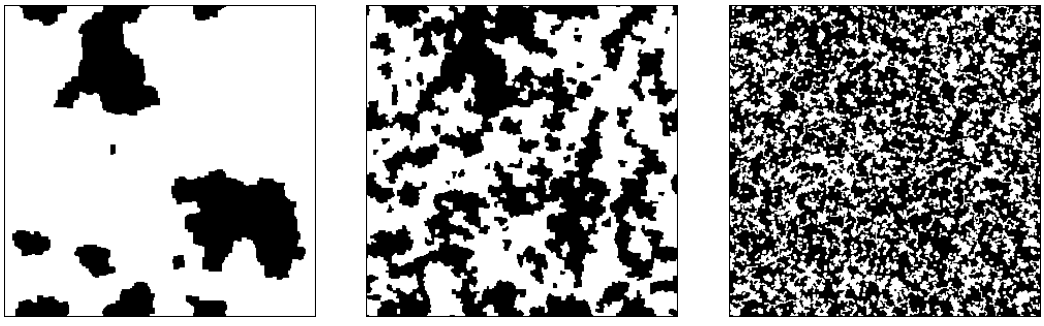

Figure 3.1: Ground states of random field Ising model with decreasing coupling constant from left to right. Black pixels represent spins with orientation "down" and white with orientation "up". In the middle, one can recognize some remnants of the left configuration.

3.3 Numerical implementation

With the Suzuki–Trotter mapping [82] the d-dimensional quantum system described by Eq. (3.3) can be represented by P coupled replicas of the classical system, Eq. (3.2) resulting in a $d+1$ dimensional classical problem with the following Hamiltonian:

$$H_{ST} = -\sum_{k=1}^{P} \left(J \sum_{\langle i,j \rangle} s_i^k s_j^k + \sum_i h_i s_i^k + J_\perp \sum_i s_i^k s_i^{k+1} \right), \tag{3.4}$$

where $J_\perp$ is the Γ -dependent coupling constant between the replicas:

$$J_\perp = -\frac{PT}{2} \ln \tanh \frac{\Gamma}{PT} \, . \tag{3.5}$$

The resulting system has periodic boundary conditions in the extra dimension. It is convenient to set periodic boundaries also for the original classical system. It should be emphasized that in the Suzuki-Trotter mapping one

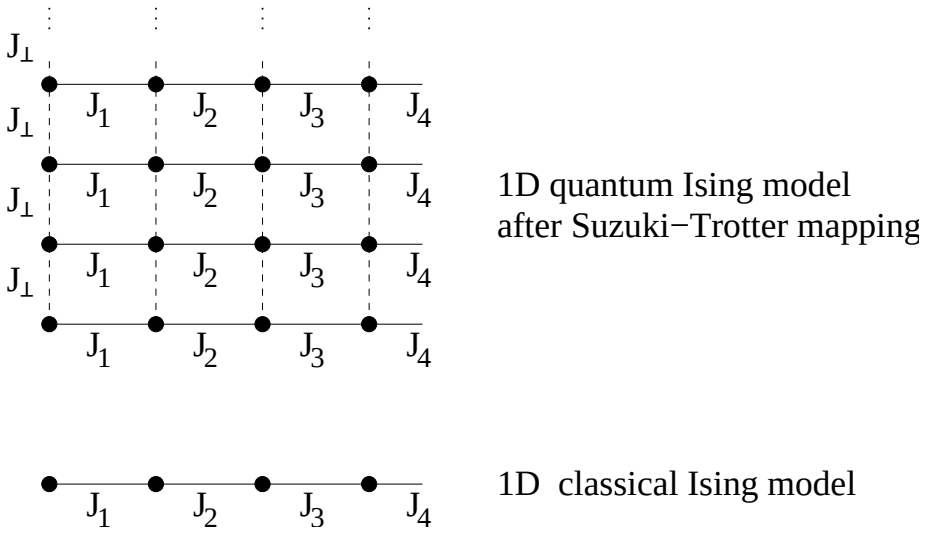

Figure 3.2: Bottom: 1d Ising model consisting of 4 spins (black dots). Top: Corresponding quantum system represented as 1+1 dimensional classical model with coupling constant $J_\perp$ denoted by the dashed line segments.

assumes that $P \to \infty$. For finite values of P there is an approximation error proportional to $O(1/(PT)^2)$ [82, 83].

The annealing of the quantum Hamiltonian (Eq. (3.3)) can be now simulated by a standard Monte Carlo sampling of Eq. (3.4) at the effective temperature PT with gradually decreasing Γ. In the computer implementation this has to be done step-wise. The total number of the (Monte Carlo) steps N_{MC} now corresponds to the annealing time τ. The residual energy e_{res} is calculated as

$$e_{res}(N_{MC}) = \langle E_{cl}(N_{MC})\rangle_k - E_{GS}, \tag{3.6}$$

where $\langle E_{cl}\rangle_k$ is the average energy of all replicas and E_{GS} is the ground state energy. The GS energy and configuration are computed for each sample, as noted in the introduction, by using a combinatorial optimization algorithm. Both $\langle E_{cl}(N_{MC})\rangle_k$ and E_{GS} from the definition in Eq. (3.6) are normalized per spin.

A priori it is naturally not clear which is the best way to reduce the value of Γ. The three following annealing schedules have been tested:

$$\Gamma_{\mathrm{Lin}}(N) = \Gamma_0(1 - \frac{N}{N_{MC}}), \tag{3.7}$$

$$\Gamma_{\mathrm{R}}(N) = \Gamma_0/(1 + R\frac{N}{N_{MC}}) \quad , \quad R = \frac{\Gamma_0}{\Gamma_f} - 1, \tag{3.8}$$

$$\begin{aligned} \Gamma_{\mathrm{Log}}(N) &= -\log\Big\{\tanh\Big[\,\mathrm{atanh}(e^{-\Gamma_0}) \\ &- \frac{N}{N_{MC}}\left(\mathrm{atanh}(e^{-\Gamma_0}) - \mathrm{atanh}(e^{-\Gamma_f})\right)\Big]\Big\}. \end{aligned} \tag{3.9}$$

The residual energies decay more or less with the same slope for all annealing schedules (Publication V). However, the logarithmic schedule (Eq. (3.9)) gives the lowest residual energy and hence the rest of the calculations are performed with this schedule only.

3.4 Convergence of the residual energy

In order to judge the performance of quantum annealing one has to be sure that the approximation error due to Suzuki-Trotter mapping does not have an effect on the convergence of the residual energy. For that purpose several

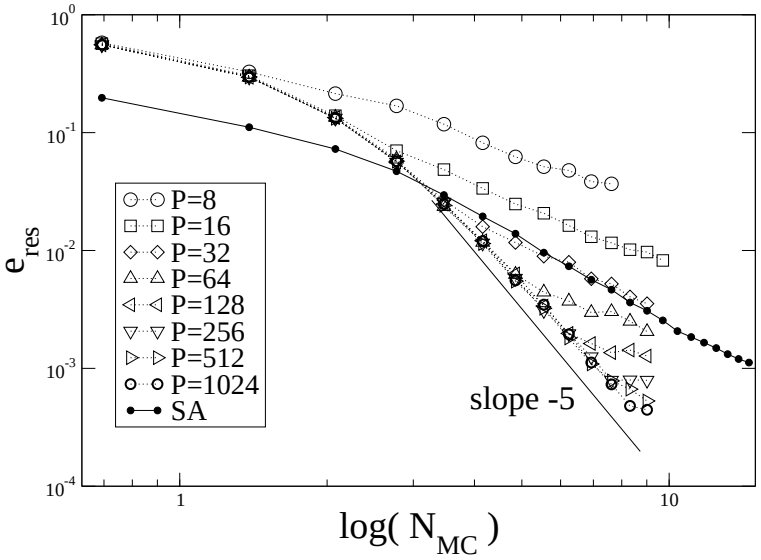

Figure 3.3: A doubly logarithmic plot of residual energies in 1d with $J = 1, L = 10^4$, $PT = 4$, $P = 8...1024$. For comparison we also show the data corresponding to the classical simulated annealing (SA). In order to compare the used Monte Carlo time, in the case of QA N_{MC} has to be multiplied with the number of replicas P.

values of P have been considered. Fig. 3.3 shows the residual energies for 1d system of 10^4 spins with $J = 1$ and $PT = 4$. The results are averaged over 10 samples. For comparison, in the same figure are presented also the residual energies obtained with SA.

When P is increased sufficiently ($P > 32$) one can observe a region where the annealing rate of QA is considerably higher compared to SA. With increasing P this region grows and we expect that this is the asymptotic behavior for $P \to \infty$. Since the Suzuki-Trotter mapping is exact in this limit, one can assume that this region reflects the properties of quantum annealing with a finite, non-zero quench rate. For finite values of P the system falls out of this quantum annealing regime to the classical Metropolis behavior as N_{MC} is increased. In the classical regime the system is fully correlated in the Trotter direction and the annealing process cannot anymore take an advantage of the extra, non-classical dimension. This means that in order to maintain a fast annealing rate for large values of N_{MC} larger P values are needed as well, as

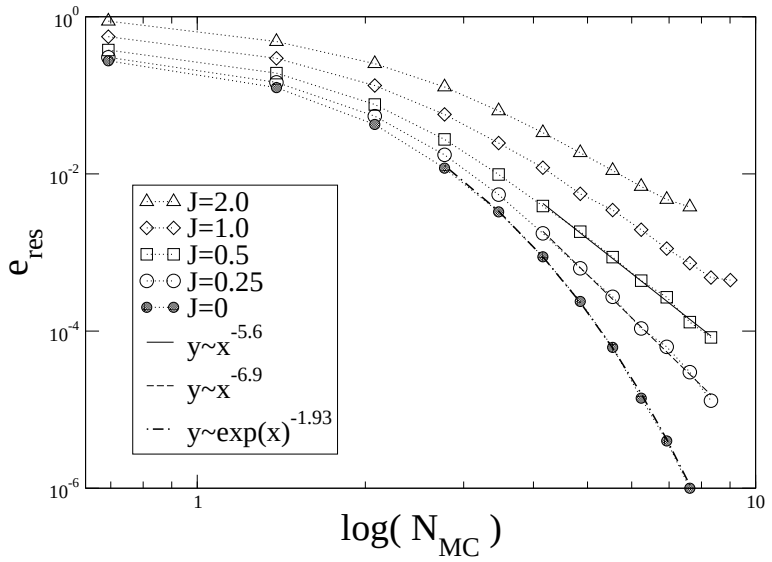

Figure 3.4: A doubly logarithmic plot of 1d residual energies, $L = 10^4$, $PT = 4$, $P = 1024$. The $J = 0$ case is a problem of L^d independent spins for which $e_{res} \sim (N_{MC})^{-\alpha}$ with $\alpha \approx 2$. For $J > 0$ e_{res} seems to decay logarithmically. With increasing J the RFIM becomes more difficult to anneal.

was also observed in Ref. [84]. Due to the finite simulation temperature the residual energy finally saturates to some non-zero value.

As indicated in Fig. 3.4 the decay rate of e_{res} depends on the actual value of the coupling constant J. The case with $J = 0$ and $\langle h^2 \rangle = 1$ is a problem of L^d independent spins for which the results depend on the used annealing schedule [85]. For the logarithmic and rational schedules we find a polynomial decay of the residual energy $e_{res} \sim (N_{MC})^{-\alpha}$ with $\alpha \approx 2$ whereas in the case of the linear annealing schedule $\alpha \approx 1$. For $J > 0$ the quantum annealing goes over to the logarithmic regime $e_{res} \sim \log(N_{MC})^{-\zeta}$. The numerical values of ζ roughly agrees with the estimate $\zeta_{max} = 6$ given by Santoro et al. [66]. As J grows, and hence the cluster sizes of the ground state, the annealing efficiency seems to diminish. When no random field is applied the dynamics of the quantum annealing in the limit $\Gamma \to 0$ for $P >> L$ corresponds to a case of a strongly anisotropic Ising model. According to Ref. [86] in the two dimensional anisotropic Ising system with $J_x >> k_B T >> J_y$ the width of the interfaces perpendicular to x–direction saturates to some finite value in

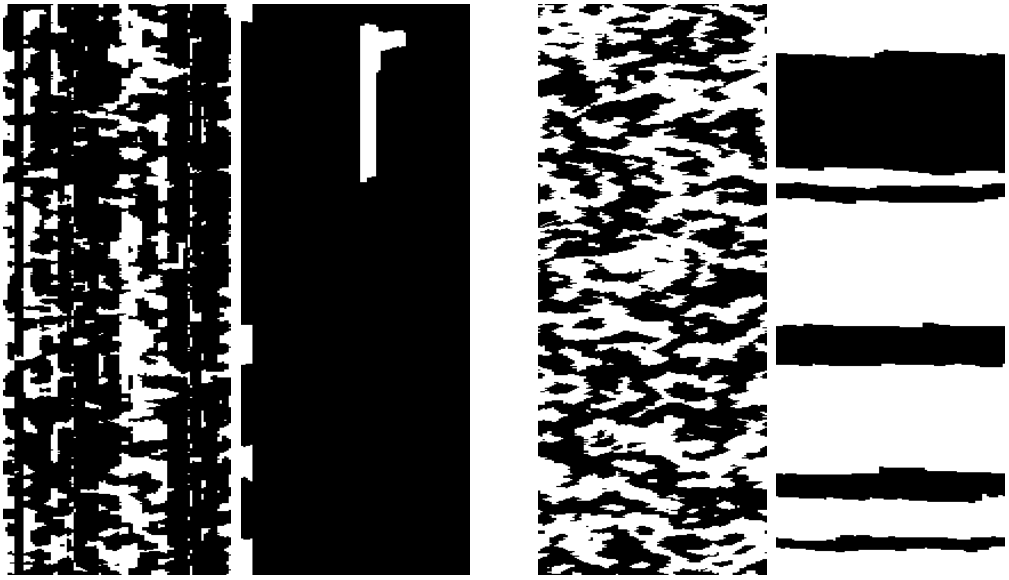

(a) (b)

Figure 3.5: The spin configurations of 1d system of size $L = 100$ after the annealing of $N_{MC} = 10$ (left) and $N_{MC} = 1000$ (right) Monte Carlo steps for the system with a finite random field (a) $[J = 2, h = 1, PT = 4, P = 1000]$ and with zero field (b) $[J = 2, h = 0, PT = 4, P = 1000]$. Black color denotes correctly aligned spins with respect to the ground state.

the large time limit. As illustrated in Fig. 3.5(b) in same limit the quantum annealing ends up in a situation where the residual energy comes from rough, fluctuating boundaries, positioned perpendicular to the Trotter direction.

For low values of J, where the size of the clusters is well below the system size, the QA performs in 2d similarly to the one dimensional case giving $\zeta \approx 6$ for $J = 0.33$ (see Fig. 3.6). With J also the cluster sizes of the ground state grow reaching the system size (128×128) approximately at $J = 1.5$. From Fig. 3.6 one can see that for $J \gtrsim 1$ one has $\zeta = 2$. Whereas in the case of one dimensional systems with extremely weak disorder the value of ζ could be raised by increasing the effective temperature PT this seems not to work in two dimensions. This suggests that there is a fundamental difference in the performance of QA depending whether the system has a disordered or ordered ground state. This conclusion is supported by the observation that with $J = 1$ for a larger system ($L = 128$, squares in Fig. 3.6) one gets lower residual energies compared to a smaller system ($L = 16$, triangles in Fig. 3.6)

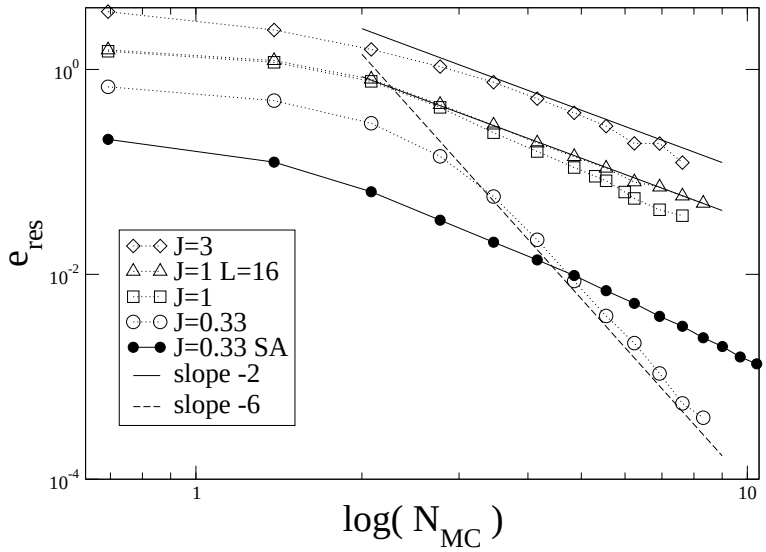

Figure 3.6: A doubly logarithmic plot of residual energies in 2d, $PT = 12$, $P = 1024$, $L = 128$, and one data set corresponding to $L = 16$. The straight lines are guides for the eye. For $J \gtrsim 1$ the residual energy decays with $\zeta \approx 2$. With growing J no further decrease of ζ is observed. For comparison see the results for classical simulated annealing (SA).

that already has an ferromagnetically ordered ground state.

The results for 3d RFIM shown in Publication V agree with the proposal that QA is sensitive to the ordering of the underlying system. For low values of J ($J < J_c \approx 0.44$ [79]) where the system is in the paramagnetic phase also at $T = 0$ we find the same QA is considerably faster than SA and ζ can be tuned towards 6 by increasing PT, whereas for a system with an ordered ground state $\zeta \approx 2$ for all values of values of PT. The general observation is that the better efficiency of QA is most clear when the ground state consists of small clusters, i.e. the correlation length of the ground state is short compared to the number of the Trotter replicas. Such benefits vanish with an increasing correlation length of the ground state configuration.

In the above analysis the residual energy e_{res} is defined as the average over all replicas (Eq.(3.6)). Alternatively, one could consider only the replica with the lowest energy. It is clear that in this case one will get lower residual energies. For $h = 0$ one would certainly end up to a zero residual energy as

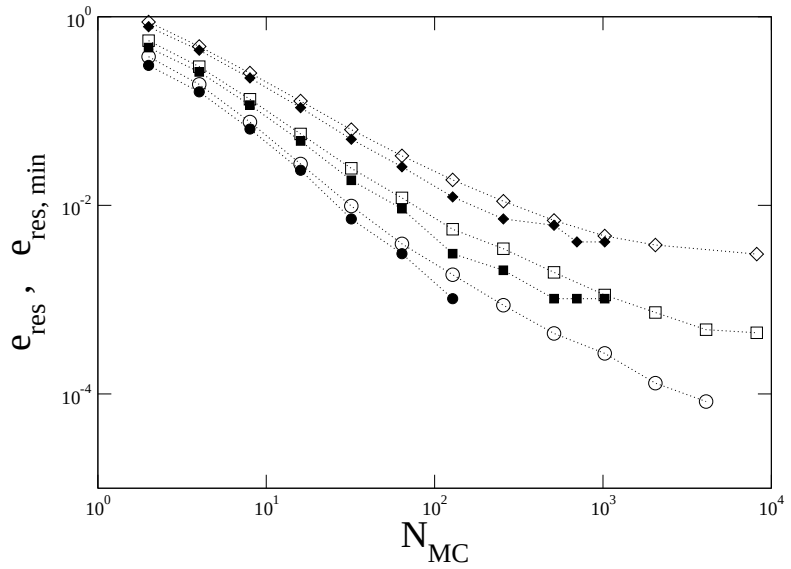

Figure 3.7: A doubly logarithmic plot of residual energies in 1d, $PT = 4$, $P = 1024$, $L = 10^4$ and $J = 0.5$ (ovals), $J = 1.0$ (squares), $J = 2.0$ (diamonds). Open symbols correspond to the residual energy $e_{\rm res}$ defined in Eq. 3.6, filled symbols correspond to the residual energy of the best replica $e_{\rm res,min}$.

it is evident from Fig. 3.5. Due to strong correlations in Trotter direction in the case of non-zero random field the residual energy is decreased only by a factor, no qualitative change in the behavior of the residual energy as a function of N_{MC} is expected. This has also been checked numerically (Fig. 3.7).

Chapter 4

Summary

This thesis provides new information about the ground state properties of systems consisting many repulsive lines. As shown in Publication I already the ground state of two lines is not separable which makes the use of a simple approximation of independent lines inappropriate. The means of combinatorial optimization make it possible to calculate efficiently the ground states of multi-line systems both in two and three dimensions. The roughening of lines in point disorder is studied in Publication II. The saturation roughness w_{sat} of 2d systems grows logarithmically with the system width L in agreement with the predictions of elastic theories [50, 51]. In 3d the saturation roughness grows linearly: $w_{sat} \sim L$ in contrast to the results coming from the elastic description [33, 42–45]. As a consequence of the individual, random walk -like wandering of lines in 3d we find that the lines get entangled. There is a transition height at which a cluster of pairwise entangled lines is formed and spans the system in the plane. Numerical evidence implies that the phenomenon is in the ordinary 2d percolation universality class (Publication III).

When point disorder is replaced by splayed columnar defects we find that the ground state is changed fundamentally (Publication IV). In contrast to point disorder it is now essentially separable which reflects up on the roughening and entanglement. Lines now exhibit a ballistic behavior (in 2d radom walk) resulting in the absence of the entanglement transition in 3d if no point disorder is included. These findings, both in point and splay disorder, are relevant for the understanding of the behavior of magnetic flux lines in type-II superconductors. It would be interesting, though not trivial, to extend the

presented studies to the lines with long range interactions which would make it possible to model systems corresponding to the Bragg glass.

The second part of the thesis considers the performance of the quantum annealing (QA) in the random field Ising model in comparison with the conventional simulated annealing (SA). Our results presented in Publication V provide direct evidence that the efficiency of QA depends on the ordering of the underlying system. When the system is in the paramagnetic phase the numerical results suggest that asymptotically QA provides a better decay rate of the residual energy $e_{res} \sim \log(N_{MC})^{-\zeta_{QA}}$ with ζ_{QA} up to 6 in agreement with the Landau-Zener -picture based scaling argument of non-adiabatic evolution [66]. This is a considerable speed-up compared to $e_{res} \sim \log(N_{MC})^{-2}$ of SA. However, when J is increased such that the ground state is ferromagnetically ordered ζ_{QA} drops to $\zeta_{QA} = 2$. This shows that the efficiency of QA depends on the ordering of the underlying system even within the same model. It still remains to be shown more rigorously why it is not possible to have adiabatic quantum annealing in the case of RFIM and what is the origin of the differences in the performance of QA in the ordered and disordered phases.

Bibliography

[1] M. Alava, P. Duxbury, C. Moukarzel, and H. Rieger, in Phase transitions and Critical phenomena, edited by C. Domb and J.L Lebowitz Academic Press, San Diego, vol 18 (2001).

[2] S. F. Edwards and P. W. Anderson, J. Phys. F **5**, 965 (1975).

[3] F. Barahona, J. Phys. A **15**, 3241 (1982).

[4] S. Kirckpatrick, C. D. Gelatt, and M. P. Vecchi, Science, **220**, 671 (1983).

[5] D. A. Huse and D. S. Fisher, Phys. Rev. Lett., **57**, 2203 (1986)

[6] M. Hirvonen, Quantum Computing, Springer (2004).

[7] T. Halpin-Healy and Y.-C. Zhang, Physics Reports **254**, 215 (1995).

[8] M. Marsili and Y.-C. Zhang, Phys. Rev. E **57**, 4814 (1998).

[9] R. Schorr and H. Rieger, Europ. Phys. J. **33**, 347 (2003).

[10] M. Kardar and Y.-C. Zhang, Phys. Rev. Lett. **58**, 2087 (1987).

[11] T. H. Cormen, C. E. Leiserson, and R. L. Rivest, Inroduction to Algorithms, Cambridge (MA) Boston, MIT press, McGraw-Hill, cop.2001

[12] A.-L. Barabasi and H. E. Stanley, *Fractal Concepts in Surface Growth* (Cambridge University Press, Cambridge, 1995).

[13] M. Kardar, Nucl. Phys. B **290** [FS20], 582 (1987).

[14] B. M. Forrest and L. H. Tang, Phys. Rev. Lett. **64**, 1405 (1990);

[15] J. M. Kim, M. A. Moore, and A. J. Bray, Phys. Rev. A **44**, 2345 (1991);

[16] N. Schwartz, A. L. Nazaryev, and S. Havlin, Phys. Rev. E **58**, 7642 (1998);

[17] E. Perlsman and S. Havlin, Phys. Rev. E **63**, 010102 (2001).

[18] D. A. Huse and C. L. Henley, Phys. Rev. Lett. **54**, 2708 (1985).

[19] E. Medina, T. Hwa, M. Kardar, and Y.-C. Zhang, Phys. Rev. A **39**, 3053 (1989).

[20] T. Halpin-Healy, Phys. Rev. A **44**, 3415 (1991).

[21] G. Zumofen, J. Klafter, and A. Blumen, Phys. Rev. A **45**, 7624 (1992).

[22] Y. Y. Goldschmidt and T. Blum, Phys. Rev. E **47**, 2979 (1993).

[23] J. M. Kim, M. A. Moore, and A. J. Bray, Phys. Rev. A **44**, 2345 (1991).

[24] Y.-C. Zhang, Phys. Rev. B **42**, 4897 (1990).

[25] K. P. J. Kytölä, E. T. Seppälä, and M. J. Alava, Europhys. Lett. **62**, 35 (2003).

[26] M. Kardar, G. Parisi, and Y. C. Zhang, Phys. Rev. Lett. **56**, 889 (1986).

[27] D. A. Huse, C. L. Henley, and D. S. Fisher, Phys. Rev. Lett. **55**, 2924 (1985)

[28] T. Nattermann and R. Lipowsky, Phys. Rev. Lett. **61**, 2508 (1988).

[29] G. Blatter, M. V. Feigel'man, V. B. Geshkenbaum, A. I. Larkin, and V. M. Vinokur, Rev. Mod. Phys. **66**, 1125 (1994).

[30] M. P. A. Fisher, Phys. Rev. Lett. **62**, 1415 (1989);

[31] D. S. Fisher et al, Phys. Rev. B **43**, 130 (1991).

[32] T. Nattermann, Phys. Rev. Lett. **64**, 2454 (1990).

[33] T. Giamarchi and P. Le Doussal, Phys. Rev. Lett. **72**, 1530 (1994).

[34] T. Giamarchi and P. Le Doussal, Phys. Rev. B **55**, 6577 (1997).

[35] B. Khaykovich, E. Zeldov, D. Majer, T. W. Li, P. H. Kes, and M. Konczykowski, Phys. Rev. Lett. **76**, 2555 (1996).

[36] K. Deligiannis, P. A. J. de Groot, M. Oussena, S. Pinfold, R. Langan, R. Gagnon, and L. Taillefer, Phys. Rev. Lett. **79**, 2121 (1997).

[37] I. Joumard, J. Marcus, T. Klein, and R. Cubitt, Phys. Rev. Lett. **82**, 4930 (1999).

[38] Y. Paltiel, E. Zeldov, Y. Myasoedov, M. L. Rappaport, G. Jung, S. Bhattacharya, M. J. Higgins, Z. L. Xiao, E. Y. Andrei, P. L. Gammel, and D. J. Bishop, Phys. Rev. Lett. **85**, 3712 (2000).

[39] Y. Nonomura and X. Hu, Phys. Rev. Lett. **85**, 5140 (2001).

[40] S. P. Obukhov and M. Rubinstein, Phys. Rev. Lett. **65**, 1279 (1990).

[41] K. V. Samokhin, Phys. Rev. Lett. **84**, 1304 (2000).

[42] T. Giamarchi and P. Le Doussal, Phys. Rev. B **52**, 1242 (1995).

[43] T. Emig, S. Bogner, and T. Nattermann, Phys. Rev. Lett. **83**, 400 (1999).

[44] S. Bogner, T. Emig, and T. Nattermann, Phys. Rev. B **63**, 174501 (2001).

[45] T. Nattermann and S. Scheidl, Advances in Physics **49**, 607 (2000).

[46] H. Rieger, Phys. Rev. Lett. **81**, 4488 (1998).

[47] L.-H. Tang, J. Stat. Phys. **77**, 581 (1994).

[48] G. Parisi, J. Phys. **51**, 1595 (1990).

[49] M. Mézard, J. Phys. **51**, 1831 (1990).

[50] J. Toner and D. P. DiVicenzo, Phys, Rev. B **41**, 632 (1990).

[51] C. Zeng, A. Alan Middleton, and Y. Shapir, Phys. Rev. Lett. **77**, 3204 (1996);

[52] D. McNamara and A. Alan Middleton, Phys. Rev. B **60** 10062 (1999).

[53] D. R. Nelson, Phys. Rev. Lett. **60**, 1973 (1988).

[54] D. R. Nelson and H. S. Seung, Phys. Rev. B **39**, 9153 (1989).

[55] B. Drossel and M. Kardar, Phys. Rev. **E** 53, 5861 (1996).

[56] F. Spitzer, Trans. Am. Math. Soc. **87**, 187 (1958).

[57] J. Rudnick and Y. Hu, J. Phys. A **20**, 4421 (1987).

[58] R. Bikbov and S. Nechaev, Phys. Rev. Lett. **87**, 150602 (2001).

[59] A. Weinrib, Phys. Rev. B **29**, 387 (1984).

[60] T. Hwa, P. Le Doussal, D. R. Nelson, and V. M. Vinokur, Phys. Rev. Lett. **71**, 3545 (1993).

[61] L. Civale, A. D. Marwick, T. K. Worthington, M. A. Kirk, J. R. Thompson, L. Krusin-Elbaum, Y. Sun, J. R. Clem, and F. Holtzberg, Phys. Rev. Lett. **67**, 648 (1991).

[62] L. Krusin-Elbaum, A. D. Marwick, R. Wheeler, C. Feild, V. M. Vinokur, G. K. Leaf, and M. Palumbo, Phys. Rev. Lett. **76**, 2563 (1996).

[63] W. K. Kwok, L. M. Paulius, V. M. Vinokur, A. M. Petrean, R. M. Ronningen, and G. W. Crabtree, Phys. Rev. Lett. **80**, 600 (1998).

[64] S. Hébert, G. Perkins, M. Abd el-Salam, and A. D. Caplin, Phys. Rev. B **62**, 15230 (2000).

[65] J. Lidmar, D. R. Nelson, and D. A. Gorokhov, Phys. Rev. B **64**, 144512 (2001).

[66] G. E. Santoro, R. Martoňák, E. Tosatti, and R. Car, Science **295**, 2427 (2002).

[67] R. Martoňák, G. E. Santoro, and E. Tosatti, Phys. Rev. E **70**, 057701 (2004).

[68] J. Brooke, T. F. Rosenbaum, and G. Aeppli, Science **284**, 779 (1999).

[69] J. Brooke, T. F. Rosenbaum, and G. Aeppli, Nature **413**, 610 (2001).

[70] D. A. Battaglia, G. E. Santoro, and E. Tosatti, Phys. Rev. E **71**, 066707 (2005).

[71] S. Suzuki and M. Okada, cond-mat/0502203.

[72] L. Stella, G. E. Santoro, and E. Tosatti, Phys. Rev. B **72**, 014303 (2005).

[73] S. R. White and A. E. Feiguin, Phys. Rev. Lett. **93**, 076401 (2004).

[74] S. Suzuki and M. Okada in "Quantum Annealing and Related Optimization Methods", Eds. A. Das and B. K. Chakrabarti, Lect. Notes in Phys., Vol. 679, Springer, Heidelberg (2005), pp 207-238.

[75] J. Dziarmaga, Phys. Rev. Lett. **95**, 245701 (2005).

[76] M. Aizenman and J. Wehr, Phys. Rev. Lett. **62**, 2503 (1989).

[77] J. Z. Imbrie, Phys Rev. Lett. **53**, 1747 (1984).

[78] J. Bricmont and A. Kupiainen, Phys. Rev. Lett. **59**, 1829 (1987).

[79] A. A. Middleton and D. S. Fisher, Phys. Rev. B **65**, 134411 (2002).

[80] E. T. Seppälä, V. Petäjä, and M. J. Alava, Phys. Rev. E **58**, R5217 (1998).

[81] E. T. Seppälä and M.J. Alava, Phys. Rev. E **63**, 066109 (2001).

[82] M. Suzuki, Prog. Theor. Phys. **56**, 1454 (1976).

[83] N. Hatano and M. Suzuki in "Quantum Annealing and Related Optimization Methods", Eds. A. Das and B. K. Chakrabarti, Lect. Notes in Phys., Vol. 679, Springer, Heidelberg (2005), pp 37-68.

[84] R. Martoňák, G. E. Santoro, and E. Tosatti, Phys. Rev. B **66**, 094293 (2002).

[85] T. Kadowaki and H. Nishimori, Phys. Rev. E, **58**, 5355 (1998).

[86] A. L. C. Ferreira, S. K. Mendiratta, and E. S. Lage, J. Phys. A: Math. Gen. **22**, L431 (1989).